



Article

Assessment and Correction of View Angle Dependent Radiometric Modulation due to Polarization for the Cross-Track Infrared Sounder (CrIS)

Joe K. Taylor ^{1,*}, Henry E. Revercomb ¹, David C. Tobin ¹, Robert O. Knuteson ¹, Michelle L. Loveless ¹, Rebecca Malloy ², Lawrence Suwinski ², Flavio Iturbide-Sanchez ³, Yong Chen ³, Glen White ⁴, Joe Predina ⁴ and David G. Johnson ⁵

¹ Space Science and Engineering Center, University of Wisconsin-Madison, Madison, WI 53706, USA

² L3Harris Technologies Inc., Fort Wayne, IN 46818, USA

³ Center for Satellite Applications and Research, National Environmental Satellite Data and Information Service, National Oceanic and Atmospheric Administration, College Park, MD 20740, USA

⁴ Logistikos Engineering LLC, Fort Wayne, IN 46845, USA

⁵ Remote Sensing Branch, Engineering Directorate, NASA Langley Research Center, Hampton, VA 23681, USA

* Correspondence: joe.taylor@ssec.wisc.edu

Abstract: The Cross-track Infrared Sounder (CrIS) is an infrared Fourier-transform spectrometer that measures the Earth's infrared radiance at high spectral resolution and high accuracy. The potential for polarization errors contributing significantly to the radiometric uncertainty of infrared remote sounders has been well recognized and documented, particularly due to polarization-dependent scene select mirrors operated in conjunction with grating-based instruments. The issue is equally applicable to FTS-based sensors. While the CrIS sensor utilizes an unprotected gold scene select mirror which has extremely low polarization in the infrared and the angle of incidence at the mirror is maintained for all calibration and Earth scene views, the radiometric bias due to polarization effects was determined to be non-negligible for cold scenes. A model for the polarization-induced calibration bias and the associated correction is presented for the CrIS instrument, along with details of the model parameter determination, and the impact of the correction on the calibrated radiances for a range of scene temperatures and types.

Keywords: calibration; Fourier-transform infrared spectroscopy; hyperspectral sensors; infrared sensors; optical polarization; remote sensing



Citation: Taylor, J.K.; Revercomb, H.E.; Tobin, D.C.; Knuteson, R.O.; Loveless, M.L.; Malloy, R.; Suwinski, L.; Iturbide-Sanchez, F.; Chen, Y.; White, G.; et al. Assessment and Correction of View Angle Dependent Radiometric Modulation due to Polarization for the Cross-Track Infrared Sounder (CrIS). *Remote Sens.* **2023**, *15*, 718. <https://doi.org/10.3390/rs15030718>

Academic Editor: Simone Lolli

Received: 25 November 2022

Revised: 7 January 2023

Accepted: 13 January 2023

Published: 26 January 2023



Copyright: © 2023 by the authors. Licensee MDPI, Basel, Switzerland. This article is an open access article distributed under the terms and conditions of the Creative Commons Attribution (CC BY) license (<https://creativecommons.org/licenses/by/4.0/>).

1. Introduction

The Cross-track Infrared Sounder (CrIS) on the Suomi NPP and NOAA-20 satellites is designed to give scientists more refined information about the Earth's atmosphere and improve weather forecasts and our understanding of climate. CrIS is an infrared Fourier-transform spectrometer (FTS) that produces high-spectral-resolution infrared radiances that provide high-resolution three-dimensional temperature and moisture profiles of the Earth's atmosphere. The highly accurate spectrally resolved infrared calibrated radiances and retrieved temperature and water vapor profiles are used to enhance weather forecasting models and have facilitated improvements to both short and long-term weather forecasting [1].

The potential for polarization errors contributing significantly to the radiometric uncertainty budget of infrared remote sounding sensors has been well recognized, particularly due to polarization-dependent scene select mirrors and for grating- and filter-based instruments [2–6]. The issue is equally applicable to FTS-based sensors.

A scene select mirror is typically used to direct calibration reference or scene radiance into a remote sensing instrument. The CrIS sensor utilizes a “barrel-roll” scene select

mirror that rotates about an axis that is 45° from the mirror normal, preserving the angle of incidence at the mirror and optical axis for all calibration and Earth scene views.

It is well known that the reflection from an inclined metallic surface will always induce some polarization. An uncoated gold scene select mirror (SSM) was chosen for CrIS due to its extremely low polarization in the infrared region. As a first-order effect, the polarization-induced by the 45° scene select mirror will be constant for all SSM rotation angles, since the incident angle at the scene mirror is constant regardless of rotation angle. The polarization associated with the other components in the instrument optical chain is not dependent on the rotation of the 45° scene mirror and is also constant for all scene mirror positions. It is expected that the sensor polarization (not including the SSM) is primarily due to the beamsplitter and aft-optic dichroics and includes small contributions from the other optical elements within the sensor. While the combined SSM and sensor polarization does not depend on SSM rotation angle, the plane of reflection at the scene mirror rotates with the scene mirror rotation and the polarization plane angle of the scene select mirror partial polarization will depend on the SSM rotation angle. The polarization sensitivity and polarization plane of the rest of the sensor optical chain is constant and independent of the SSM rotation angle. As a result, it can be understood that the rotation of the reflection plane at the scene mirror will create a small polarization-induced modulation of the signal measured at the detector.

An assessment of the SNPP CrIS radiometric uncertainty (RU) was completed by Tobin et al. [7] shortly after the launch of SNPP. Radiometric uncertainty characterizes the accuracy of the observed radiance spectra and represents an upper limit of the bias with respect to the true radiance and does not include effects such as detector noise which vary randomly from one spectrum to another. The RU was assessed via perturbation of the calibration equation, following accepted metrology approaches and the resulting on-orbit SNPP CrIS RU estimates for Earth view spectra were shown to be less than 0.2 K 3-sigma in the midwave and shortwave bands, and less than 0.3 K 3-sigma in the longwave band [7]. Applying the same radiometric uncertainty assessment described by Tobin to the NOAA-20 CrIS sensor (Figure 1) shows that it has similar or better RU performance to SNPP, except for midwave field of view (FOV) 9 that has an anomalously large non-linearity. Two distributions are evident in the NOAA-20 midwave RU shown Figure 1, one with larger RU (associated with midwave FOV 9), and one that is quite similar in shape and magnitude to the SNPP midwave RU distribution.

Early polarization analysis prior to the launch of SNPP CrIS only considered transmission effects and indicated that calibration bias due to polarization was expected to be insignificant for CrIS and that a correction did not need to be included in the calibration. Accordingly, polarization was not expected to be a significant contributor to radiometric uncertainty and was not included in the calibration algorithm or in the original SNPP RU assessment. However, when the polarized infrared emission from the scene mirror is considered in addition to the transmission effects, the view angle dependent radiometric modulation due to polarization becomes significant for CrIS for cold scenes and including a correction for this effect in calibration is warranted. In fact, the magnitude of the polarization correction is larger than the total radiometric uncertainty due to all other contributors in parts of the midwave and shortwave bands for cold scenes when left uncorrected.

This document is divided into six sections. An introduction to the CrIS instrument and the issue of view angle dependent calibration bias associated with polarization has been provided in this section. Section 2 provides a brief review of the mathematical representation of polarized light and the polarization ellipse and introduces the conceptual model which represents the scene select mirror and sensor as a series pair of partial linear polarizers. In Section 3, the mathematical model of the polarization-induced calibration bias is presented along with an estimate of the potential bias for the CrIS sensor. Section 4 describes the methodology used to estimate the required polarization parameters from the CrIS data acquired during the SNPP and NOAA-20 pitch maneuvers conducted in February 2012 and January 2018, respectively. Section 5 presents results for the correction of

view angle dependent radiometric modulation due to polarization for the CrIS instrument and updates the radiometric uncertainty estimate to include the contribution associated with the uncertainty in polarization correction. Section 6 summarizes the impact of the CrIS polarization correction on comparisons between CrIS and other instruments and a summary of the current status and future work is provided in Section 7.

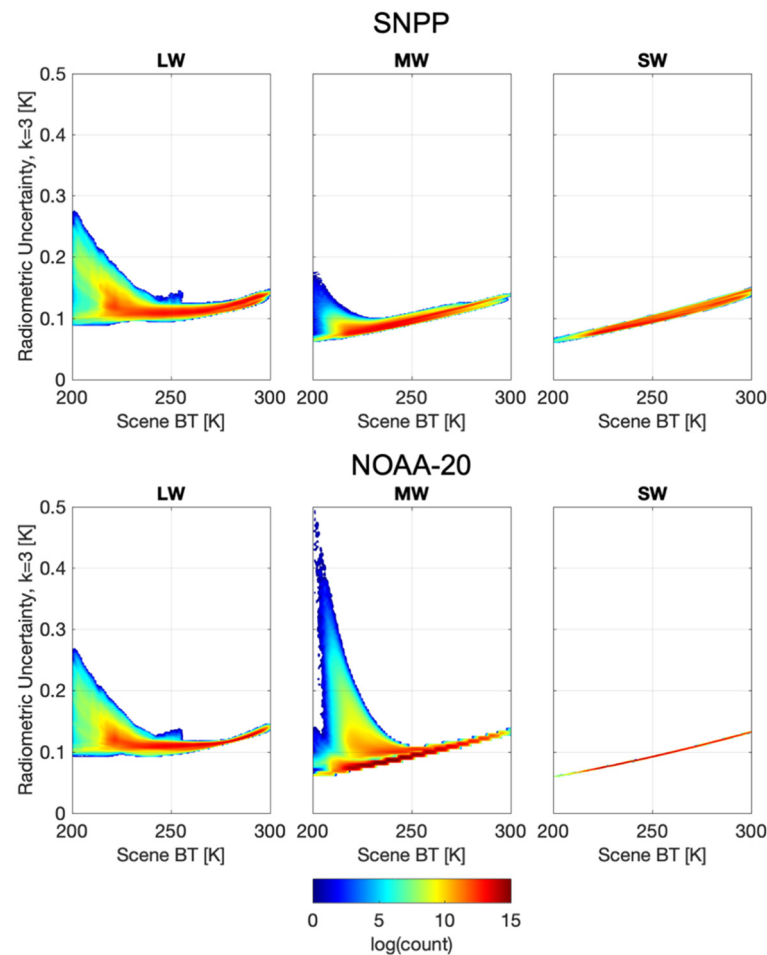


Figure 1. Radiometric uncertainty (RU) for one orbit of data from the SNPP (top) and NOAA-20 (bottom) Cross-track Infrared Sounder (CrIS) consistent with the methodology and uncertainty contributors originally described by Tobin et al. [7] for SNPP. Two distributions are evident in the NOAA-20 midwave (MW) RU, one with larger RU (associated with MW FOV 9), and one that is quite similar in shape and magnitude to the SNPP MW RU distribution. Polarization was not expected to be a significant contributor to radiometric uncertainty and was not included in the original SNPP RU assessment and has not been included in these results for consistency with the original SNPP analysis. Updated radiometric uncertainty estimates including the contribution associated with the uncertainty in polarization correction are provided in Section 5.

2. Theory

2.1. The Polarization Ellipse

It is useful to begin with a brief review of the mathematical representation of polarized light and the polarization ellipse. The reader is referred to Hecht [8], Collett [9], or Goldstein [10] for a more detailed explanation of the material summarized here.

Light can be represented mathematically in terms of the x- and y-axis projections of the transverse electrical field vector, for light propagating parallel to the z-axis. The propagation of the transverse field is shown in Figure 2.

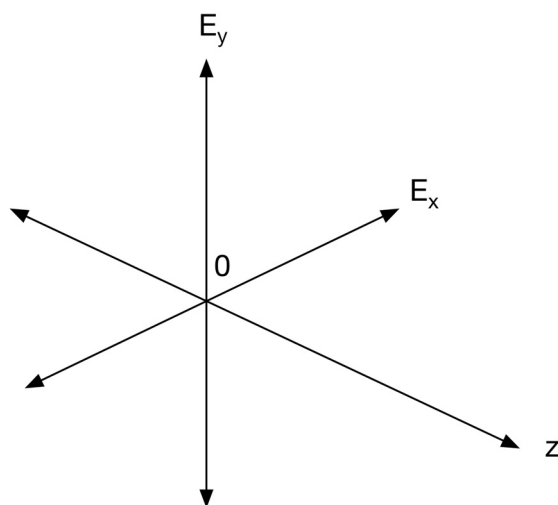


Figure 2. Propagation of the transverse optical field [10].

The transverse components are given by:

$$E_x(z, t) = E_{0x} \cos(\tau + \delta_x) \tag{1}$$

$$E_y(z, t) = E_{0y} \cos(\tau + \delta_y) \tag{2}$$

In Equations (1) and (2), $\tau = \omega t - kz$ is the space-time propagator, where ω is the angular frequency and k is the wave vector; the subscripts x and y indicate the directions of the transverse axes, E_{0x} and E_{0y} are the maximum amplitudes of the projection of the electric field vector on the x and y axes; and δ_x, δ_y are the corresponding phases. The pattern traced out by the tip of the electric field vector in the x - y plane is described by:

$$\frac{E_x^2}{E_{0x}^2} + \frac{E_y^2}{E_{0y}^2} - 2 \frac{E_x E_y}{E_{0x} E_{0y}} \cos \delta = \sin^2 \delta \tag{3}$$

In (3), $\delta = \delta_y - \delta_x$ is the phase difference between the two components and the time-space propagator has been explicitly eliminated. Regardless, the electric field components E_x and E_y continue to be space and time dependent, and space and time define an instant on the curve described by (3).

Equation (3) describes an ellipse with the major axis at an angle ψ to the x -axis, and is referred to as the polarization ellipse. The polarization ellipse can also be expressed in terms of the orientation angle ψ ($0 \leq \psi \leq \pi$) and the ellipticity angle χ ($-\pi/4 < \chi \leq \pi/4$). These angles can be defined in terms of the parameters of the polarization ellipse [2,3]:

$$\tan(2\psi) = \frac{2E_{0x}E_{0y}}{E_{0x}^2 - E_{0y}^2} \cos \delta \tag{4}$$

$$\sin(2\chi) = \frac{2E_{0x}E_{0y}}{E_{0x}^2 + E_{0y}^2} \sin \delta \tag{5}$$

Equations (4) and (5) can be expressed as purely geometrical equations via the introduction of the auxiliary angle α , which represents the relation between E_{0x} and E_{0y} :

$$\tan(2\psi) = \tan(2\alpha) \cos \delta \tag{6}$$

$$\sin(2\chi) = \sin(2\alpha) \sin \delta \tag{7}$$

where

$$\tan \alpha = \frac{E_{0y}}{E_{0x}} \tag{8}$$

The limits on α and δ in (6) and (7) are $0 \leq \alpha \leq \pi/2$ and $0 \leq \delta < 2\pi$. The rotated polarization ellipse is shown in Figure 3.

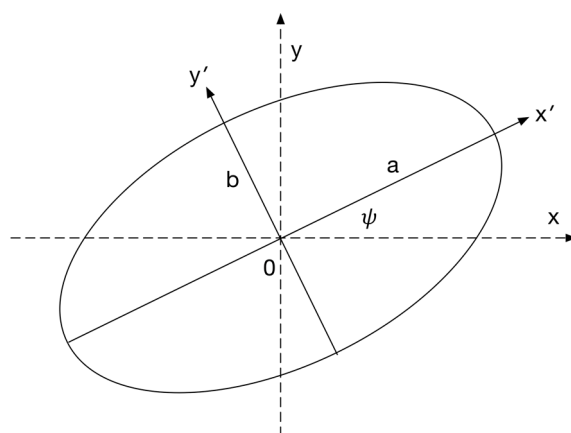


Figure 3. The rotated polarization ellipse [10].

2.2. Calibration Bias due to Polarization

When considering the calibration bias due to polarization, representing the scene select mirror and sensor as a series pair of partial linear polarizers helps provide insight into the problem. This is illustrated in Figure 4. The first polarizer represents the polarization due to the scene select mirror and the second polarizer represents the sensor contribution. The sensor polarization sensitivity includes contributions from all optical components within the sensor beyond the scene select mirror.

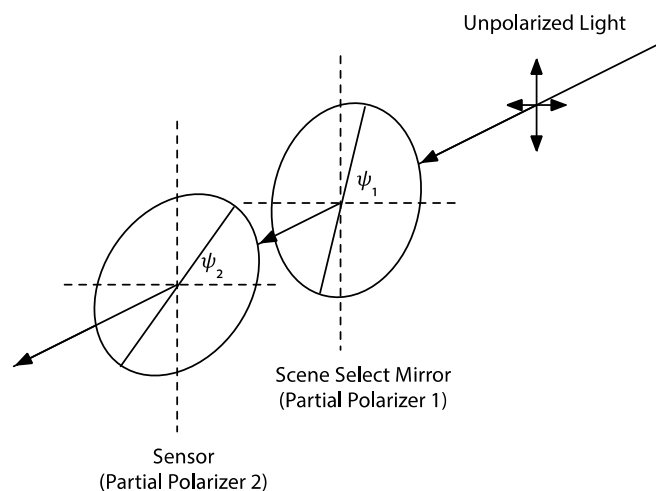


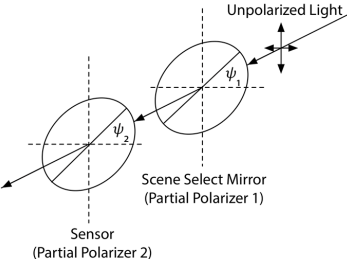
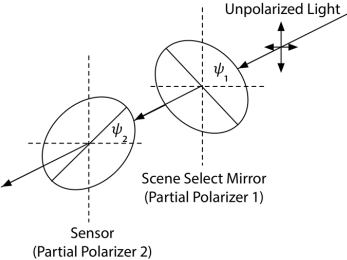
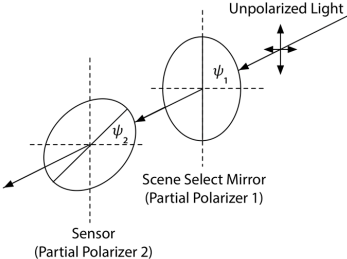
Figure 4. Representing the scene select mirror and sensor as a series pair of partial polarizers is useful when considering the calibration bias due to polarization. The first polarizer represents the scene select mirror, and the second polarizer represents the combined instrument polarization sensitivity due to the rest of the optical components within the sensor.

The CrIS instrument uses a scene select mirror to direct radiance from the calibration references (Internal Calibration Target, ICT and deep space, DS), and the Earth scene (at multiple cross-track angles) into the instrument. Mirrors inherently introduce polarization that depends both on the angle of incidence and the orientation of the mirror. Unprotected gold was selected for the CrIS scene select mirror as it causes an extremely small level of signal polarization upon reflection for the infrared spectral region that CrIS covers. The CrIS sensor employs a 45° scene mirror rotated about the local optical axis such that the incident angle at the scene mirror is independent of scene mirror rotation angle. Thus, the

amount of partial polarization introduced by the scene mirror is constant and independent of scene mirror rotation angle. If this were the only consideration, the polarization effects would cancel in the standard calibration equation. However, the orientation of the partial polarization introduced by the scene select mirror does depend on the rotational position of the scene select mirror. The instrument also has a polarization sensitivity, which is primarily due to the beamsplitter and aft-optic dichroics, but also includes small contributions from the other optical elements within the sensor. The polarization sensitivity and polarization plane of the instrument is constant and independent of the scene mirror rotation angle.

While the level of polarization is constant for the scene select mirror and sensor individually, the combined polarization due to the scene select mirror and the sensor is a function of the relative angle between the scene select mirror polarization axis at angle ψ_1 , which changes with rotation of the scene select mirror, and the instrument polarization axis, which is fixed and oriented at a constant angle, ψ_2 . Thus, the combined polarization depends on the scene mirror rotation angle, and the rotation of the reflection plane at the scene mirror will create a modulation of the measured signal. When the major axes of the polarization ellipses for the scene select mirror and sensor are aligned, transmission of unpolarized light is at a maximum (T_{max}). When they are perpendicular, the transmission is at a minimum (T_{min}). For a 360° rotation of the scene select mirror, there will be two maxima and two minima. For the same 360° scene select mirror rotation, there will also be four scene select mirror angles for which the major axes of the polarization ellipses are at 45° to one another. At these angles, the transmission will be the mean of the minimum and maximum response. A summary of these conditions is provided in Table 1.

Table 1. Relative orientation of scene select mirror and sensor polarizations and resulting transmission for unpolarized light.

Illustration	Relative Orientation of SSM and Sensor Polarization	Transmission of Unpolarized Light
	$ \psi_1 - \psi_2 = 0^\circ$ $ \psi_1 - \psi_2 = 180^\circ$	T_{max}
	$ \psi_1 - \psi_2 = 90^\circ$ $ \psi_1 - \psi_2 = 270^\circ$	T_{min}
	$ \psi_1 - \psi_2 = 45^\circ$ $ \psi_1 - \psi_2 = 135^\circ$ $ \psi_1 - \psi_2 = 225^\circ$ $ \psi_1 - \psi_2 = 315^\circ$	$\frac{1}{2}(T_{max} + T_{min})$

3. Polarization-Induced Calibration Biases

3.1. Polarization-Induced Calibration Bias Theoretical Model

In this section, a theoretical model of the polarization-induced calibration bias is presented for the CrIS instrument, which follows the approach used by Taylor [11,12] for the Absolute Radiance Interferometer (ARI) and Pagano [3] for the Atmospheric Infrared Sounder (AIRS). Like the CrIS instrument, the ARI and AIRS sensors utilize a barrel-roll scene mirror that rotates about an axis that is 45° from the mirror normal, preserving the angle of incidence of the mirror and optical axis for all scene views. An uncoated gold scene select mirror was chosen for both CrIS and ARI due to its extremely low polarization in the infrared, while AIRS employs a Denton silver scene mirror with a SiO_2 protective coating [13], which has a significantly larger polarization than unprotected gold in the infrared. Key steps in the derivation of the expression for the calibration bias due to polarization are included in this section.

As noted earlier, the orientation of the polarization axis of the scene select mirror rotates with scene mirror. When coupled with the polarization sensitivity of the sensor, this produces a radiometric modulation of the detected signal that is dependent on the rotation angle of the scene select mirror.

For this problem, we assume that the instrument has a polarization dependent transmission and the scene select mirror has a polarization dependent reflectance. It is also assumed that both the scene select mirror and the instrument are adequately represented as simple linear polarizers and form a polarizer-analyzer pair. Equation (9) describes the total signal intensity generated for an arbitrary, unpolarized scene or calibration radiance observed at a scene selection mirror angle δ and a sensor polarization axis at an angle α . Note that the individual intensity terms in (9) follow from squaring the components of the scene selection mirror p-polarization and s-polarization amplitudes along both the maximum and minimum axis of the instrument transmission.

$$\begin{aligned}
 V_\delta = & \frac{L_\delta}{2} r_p [t_{\max} \cos^2(\delta - \alpha) + t_{\min} \sin^2(\delta - \alpha)] \\
 & + \frac{L_\delta}{2} r_s [t_{\max} \sin^2(\delta - \alpha) + t_{\min} \cos^2(\delta - \alpha)] \\
 & + \frac{B_{SSM}}{2} \varepsilon_p [t_{\max} \cos^2(\delta - \alpha) + t_{\min} \sin^2(\delta - \alpha)] \\
 & + \frac{B_{SSM}}{2} \varepsilon_s [t_{\max} \sin^2(\delta - \alpha) + t_{\min} \cos^2(\delta - \alpha)] \\
 & + V_{inst}
 \end{aligned} \tag{9}$$

In (9), r_p and r_s are the reflectivity (not the reflection coefficients, which act on the field) of the scene mirror for the parallel and perpendicular polarization states, respectively; ε_p and ε_s are the corresponding emissivities and are equal to $1 - r_p$ and $1 - r_s$, since the transmittance for a metal mirror is zero; t_{\max} , t_{\min} are respectively the intensity transmission on the major and minor axis of the instrument polarization ellipse, with the major axis oriented at angle α , and both α and δ are specified with respect to the nadir view (refer to Figure 5), and V_{inst} is the detector preamp output voltage due only to instrument background radiance and detector dark current. The model depends on the relative orientation of the scene mirror and sensor polarization axes, not the absolute angular position of either. Hence, the choice of the 0° position is arbitrary, and the angular position of the nadir view was chosen as the 0° reference for convenience. The total signal, V_δ , at scene mirror angle δ is composed of the scene radiance L_δ as attenuated by the scene mirror reflectance, and the radiant emission from the scene mirror, where B_{SSM} is a radiance from a blackbody at the temperature of the scene selection mirror. Both contributions are polarized after reflection or emission from the scene select mirror, and are thus transmitted differently by the instrument, which has a polarization dependent transmission. In this section, we are interested in modeling the polarization induced calibration bias. Thus, for simplicity we have assumed the responsivity is unity in (9), since that term will divide out when the signals are substituted into the radiometric calibration equation.

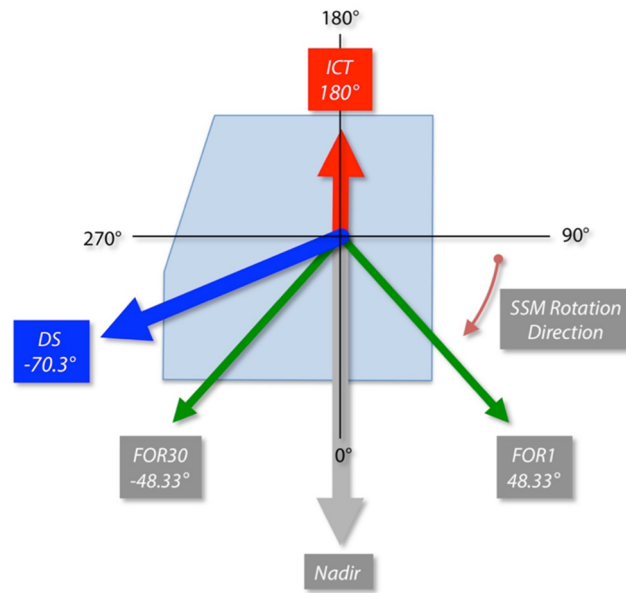


Figure 5. The coordinate system used for the sensor polarization angle (α) and the scene selection mirror angle (δ) is illustrated. The model depends on the relative orientation of the scene mirror and sensor polarization axes, not the absolute angular position of either. Hence, the choice of the 0° position is arbitrary, and the angular position of the nadir view was chosen as the 0° reference for convenience.

Using geometric identities, one can show:

$$\begin{aligned} a \cdot \cos^2(\theta) + b \cdot \sin^2(\theta) &= \frac{1}{2}(a+b)[\cos^2(\theta) + \sin^2(\theta)] \\ &\quad + \frac{1}{2}(a-b)[\cos^2(\theta) - \sin^2(\theta)] \\ &= \frac{1}{2}(a+b) + \frac{1}{2}(a-b)\cos(2\theta) \end{aligned} \quad (10)$$

and (9) can be re-written as,

$$\begin{aligned} V_\delta &= \left[(L_\delta - B_{SSM})\frac{1}{2}(r_p + r_s) + B_{SSM} \right] \frac{1}{2}(t_{\max} + t_{\min}) \\ &\quad + (L_\delta - B_{SSM})\frac{1}{2}(r_p - r_s)\frac{1}{2}(t_{\max} - t_{\min})\cos 2(\delta - \alpha) \\ &\quad + V_{inst} \end{aligned} \quad (11)$$

Finally, Equation (11) can be further simplified:

$$\begin{aligned} V_\delta &= (L_\delta - B_{SSM})rt + B_{SSM}t \\ &\quad + (L_\delta - B_{SSM})p_r p_t r t \cos 2(\delta - \alpha) + V_{inst} \end{aligned} \quad (12)$$

where

$$r = \frac{1}{2}(r_p + r_s) \quad (13)$$

$$t = \frac{1}{2}(t_{\max} + t_{\min}) \quad (14)$$

$$p_r = \frac{r_p - r_s}{r_p + r_s} \quad (15)$$

$$p_t = \frac{t_{\max} - t_{\min}}{t_{\max} + t_{\min}} \quad (16)$$

In (12) through (16) r is the scene select mirror reflectance, t is the sensor transmittance, p_t is the scene select mirror polarization, and p_r is the sensor polarization. An expression for the polarization-induced calibration error can be derived by substituting the expression for the total signal generated for an arbitrary, unpolarized scene or calibra-

tion radiance observed at a scene selection mirror angle defined in (12) into the complex calibration equation.

The complex calibration method developed by Revercomb et al. [14] is used for the CrIS radiometric calibration. The basic radiometric calibration expression for this method is

$$L_S = (L_{ICT} - L_{DS}) \operatorname{Re} \left\{ \frac{\mathbb{S}_S - \mathbb{S}_{DS}}{\mathbb{S}_{ICT} - \mathbb{S}_{DS}} \right\} + L_{DS} \quad (17)$$

In (17) L_S is the calibrated radiance; \mathbb{S}_S , \mathbb{S}_{DS} and \mathbb{S}_{ICT} are the complex measured spectra for the scene, deep space reference, and internal calibration target (ICT) calibration reference views respectively after correction for any nonlinear instrument response; L_{DS} and L_{ICT} are the calculated radiances for the respective deep space and ICT calibration reference views; and $\operatorname{Re}\{\dots\}$ denotes the real part of the complex number. While these quantities are spectrally resolved and a function of wavenumber σ , the explicit dependence on wavenumber has been omitted from the equation to simplify notation. Radiances are expressed in units of $\text{mW}/(\text{m}^2 \cdot \text{sr} \cdot \text{cm}^{-1})$, and the wavenumber scale is specified in units of cm^{-1} . The calculated radiance from a non-ideal blackbody cavity such as the ICT is the sum of the emitted and reflected radiance from the cavity. There has been no evidence of any issues with or obstruction of the CrIS deep space view, and thus $L_{DS} \cong 0$ and (17) can be further simplified to:

$$L_S = L_{ICT} \operatorname{Re} \left\{ \frac{\mathbb{S}_S - \mathbb{S}_{DS}}{\mathbb{S}_{ICT} - \mathbb{S}_{DS}} \right\} \quad (18)$$

Note that Equations (17) and (18) represent the radiometric portion of the CrIS calibration. Spectral calibration, including the correction of self-apodization effects, and resampling to the output wavenumber sampling are also included in the CrIS calibration [15], but the basic radiometric calibration expression is all that is required for the derivation of the polarization correction. A relationship between the correct calibrated radiance L_S and the calibrated radiance affected by the calibration bias due to polarization $L_{\delta,S}$ can be defined:

$$\begin{aligned} L_{\delta,S} &= L_S + E_p^\delta \\ L_S &= L_{\delta,S} - E_p^\delta \end{aligned} \quad (19)$$

where E_p^δ is the polarization induced error and is dependent on scene selection mirror angle δ . Accordingly, the polarization correction is $-E_p^\delta$, equal in magnitude and opposite in sign of the calibration bias due to polarization. As noted previously, the radiometric bias due to polarization depends on the relative orientation of the scene mirror and sensor polarization axes, not the absolute angular position of either. Since the sensor polarization α is constant, to simplify notation only the dependence on the scene mirror angle δ is explicitly indicated in Equation (19).

Substituting (12) into (18), and assuming non-complex spectral measurements for simplicity,

$$L_{\delta,S} = L_{ICT} \left[\frac{V_{\delta,S} - V_{\delta,DS}}{V_{\delta,ICT} - V_{\delta,DS}} \right] \quad (20)$$

While (20) does not explicitly represent the real and imaginary nature of raw spectra and the complex calibration methodology, that complication is not needed to characterize the radiometric error due to polarization. As noted previously, the radiometric bias due to polarization depends on the relative orientation of the scene mirror and sensor polarization axes, not the absolute angular position of either. Since the sensor polarization α is constant, to simplify notation only the dependence on the scene mirror angle δ is explicitly indicated in Equations (19) and (20).

The total signal V_δ generated for an arbitrary, unpolarized scene or calibration radiance observed at a scene selection mirror angle δ is provided in Equation (12), and can be substituted into Equation (20) for the scene ($V_{\delta,S}$), deep space calibration reference ($V_{\delta,DS}$),

and ICT calibration reference ($V_{\delta,ICT}$) measurements, to derive an expression for the calibration bias due to polarization E_p^δ .

$$E_p^\delta \cong p_r p_t \left\{ \begin{array}{l} L_S \cos 2(\delta - \alpha) - L_S \cos 2(\delta_{ICT} - \alpha) \\ -B_{SSM} \left[\begin{array}{l} \cos 2(\delta - \alpha) - \frac{L_S}{L_{ICT}} \cos 2(\delta_{ICT} - \alpha) \\ -\frac{L_{ICT} - L_S}{L_{ICT}} \cos 2(\delta_{DS} - \alpha) \end{array} \right] \end{array} \right\} \quad (21)$$

For CrIS, cross-track coverage is required, and the radiometric bias due to polarization cannot be eliminated for all Earth fields of regard (FORs) by design. Accordingly, a correction is required if the polarization induced calibration error is a significant contributor to the radiometric uncertainty. With accurate parameterization Equation (21) can be used to correct for the calibration bias due to polarization for the CrIS instrument. For calculation of the correction, L_S in Equation (21) is approximated by $L_{\delta,S}$. Using the sensor dependent polarization parameters described in detail in the following sections, the maximum percentage difference in E_p^δ due to the approximation is 0.11% for NOAA-20, and 0.13% for SNPP. When expressed in brightness temperature units, the maximum error in the calculation of E_p^δ due to the approximation is 0.05 K for NOAA-20 and 0.08 K for SNPP. The small sensor dependent differences in approximation error are due to the slightly different polarization parameters for the two sensors. Thus, this is an acceptable approximation when calculating the polarization correction since the error associated with this approximation is insignificant with respect to the size of the correction.

For accurate and effective derivation of the polarization parameters and an accurate correction of a calibration bias due to polarization, it is important to identify the expected spectral, field of view (FOV), and field of regard (FOR) dependence of the polarization of the scene select mirror and sensor, and sensor polarization axis. It is evident from Equation (21) that the calibration bias due to polarization depends on the combined SSM and sensor polarization, the scene mirror rotation angle for the scene and calibration reference views, the sensor polarization angle, the scene mirror temperature, and the scene and ICT radiances. Component level measurements indicate that the combined SSM and sensor polarization ($p_r p_t$) will have a low frequency spectral dependence in all detector bands with no high spectral resolution features. The effective polarization angle of the sensor (α) is expected to primarily depend on the beamsplitter and the aft-optic dichroics and tilted windows. Accordingly, it will have a detector band dependence due to differences in aft-optic dichroics between the three bands. Additionally, the combined SSM and sensor polarization, sensor polarization angle, and effective scene mirror rotation angle (δ) are also expected to have a small FOV dependence since each detector has a slightly different optical path through the sensor and incident angles at each optical surface. Finally, due to optical coating differences between SNPP and NOAA-20, the two sensors will have small differences in their polarization parameters.

Note that for the Absolute Radiance Interferometer (ARI) [12,16,17], one of the goals of the optical design was to eliminate the polarization induced calibration error, E_p^δ . Since there is no cross-track coverage requirement for the ARI and it has a single on-axis detector for each band, this can be accomplished by separating the calibration references, verification source, and nadir viewport by 90° in scene select mirror rotation with each located 45° from the instrument polarization plane. Thus, $\delta_{DS} - \alpha$, $\delta_{ICT} - \alpha$, $\delta_S - \alpha$ are all equal to 45° , and all of the $\cos 2(\delta - \alpha)$ terms are zero, resulting in $E_p^\delta = 0$ for Equation (21).

3.2. Modeling CrIS Polarization-Induced Calibration Error

To demonstrate and better understand the nature and potential calibration bias due to uncorrected polarization, a model based on Equation (21) was created, and reasonable preliminary model input values were defined for the initial assessment. For simplicity, spectrally independent estimates for instrument polarization and scene select mirror polarization that were representative of the predicted band averaged values based on CrIS component level measurements were used for the preliminary model ($p_r = 0.0055$, $p_t = 0.08$).

Other approximations used in the preliminary model included a completely isothermal instrument with the same SSM, instrument, and ICT temperatures; ideal blackbody radiances; and a sensor polarization angle (α) value of 0° for all bands. A sensor polarization angle of 0° corresponds to the simplest case for the CrIS optical geometry in which the aft optics do not contribute significantly to the sensor polarization angle, and the sensor polarization angle is due only to the interferometer beamsplitter. Actual values for α were later determined from the CrIS on-orbit pitch maneuver data which permitted all Earth scene scan positions to view deep space. From this data it was confirmed that the aft optic dichroics had a significant contribution to the sensor polarization angle for the longwave and midwave detector bands. The preliminary input parameters for the polarization model results presented in this section are summarized in Table 2.

Table 2. Preliminary polarization parameters used for initial model.

Description		Value	Notes
Temperatures			
Cold Cal Ref, Deep Space View (DS)	T_{DS}	2.8 K	Effective brightness temperature of the DS view
Hot Cal Ref, Internal Calibration Target (ICT)	T_{ICT}	282 K	Should represent typical on-orbit temperature
Earth Scene or External Target Temperature	T_S	210–330 K	
SSM Temperature			
Reflected Radiance, Cold Cal Ref	$T_{R,DS}$	282 K	Average instrument background temperature
Reflected Radiance, Hot Cal Ref	$T_{R,ICT}$	282 K	
Reflected Radiance, Scene or Ext. Target	$T_{R,S}$	282 K	
Emissivities			
Cold Cal Ref, Deep Space View, (DS)	e_{DS}	1	A perfect DS view will have an effective emissivity of unity
Hot Cal Ref, Internal Cal Target (ICT)	e_{ICT}	1	Set to unity for initial model
Earth Scene	e_S	1	Set to unity for initial model
Polarization			
Instrument polarization ellipse, angle	α	0°	The model depends on $\delta - \alpha$, not the absolute angular position of either δ or α . Hence, the choice of the 0° position is arbitrary, and the angular position of the nadir view was chosen as the 0° reference for convenience.
Cold Cal Ref (DS) Position (Nominal)	δ_{DS}	-70.3°	
Hot Cal Ref (ICT) Position (Nominal)	δ_{ICT}	180°	
Cross-track FOR Angles (Nominal)	δ_S	-48.33° to 48.33°	

The resulting modelled polarization induced calibration error at 900 cm^{-1} , 1500 cm^{-1} , and 2300 cm^{-1} as a function of scene brightness temperature and scene select mirror angle is plotted in Figure 6. Several important characteristics of the calibration error due to polarization are illustrated by this figure. With a sensor polarization angle of 0° , ICT angle of 180° , and deep space view angle of -70.3° , the peak calibration error occurs at and is symmetric about nadir (0°). As expected, the magnitude of the polarization induced calibration error increases as the difference between the scene temperature and the instrument temperature increases, the calibration bias is positive for scenes colder than the instrument and negative for scenes warmer than the instrument, and the largest calibration error corresponds to the coldest scene in the figure. Furthermore, since the ICT has been approximated as a perfect blackbody with the ICT at the same temperature as the SSM, it is obvious from inspection of Equation (21) that the calibration bias due to polarization will be exactly zero when the scene temperature is equal to the ICT temperature under these assumptions. The near zero calibration bias at all wavenumbers for the 280 K scene in Figure 6 clearly illustrates this characteristic of the calibration bias due to polarization. Finally, while spectrally independent estimates for instrument polarization and scene select mirror polarization have been used in the preliminary model, because of the spectral dependence of the Planck function, when expressed in brightness temperature units the calibration errors are larger for shorter wavelengths. The peak calibration error for a 210 K

scene brightness temperature is approximately +0.1 K at 900 cm^{-1} , +0.2 K at 1500 cm^{-1} , and outside the scale of the plot (+0.56 K) at 2300 cm^{-1} , respectively. While the CrIS radiometric accuracy specification is expressed as a percent radiance uncertainty with respect to a 287 K Planck radiance for scenes with an equivalent brightness temperature range of 233 K through 287 K, a wider range of scene brightness temperatures (210–330 K) is plotted in Figure 6 to include Earth scenes with more extreme equivalent brightness temperatures. The peak calibration error for a 230 K scene brightness temperature is approximately +0.06 K at 900 cm^{-1} , +0.09 K at 1500 cm^{-1} , and +0.16 K at 2300 cm^{-1} . It is clear from Figures 1 and 6 that the magnitude of the radiometric bias due to polarization (for these model parameters) is larger than the total radiometric uncertainty due to all other contributors in parts of the midwave and shortwave bands for cold scenes when left uncorrected.

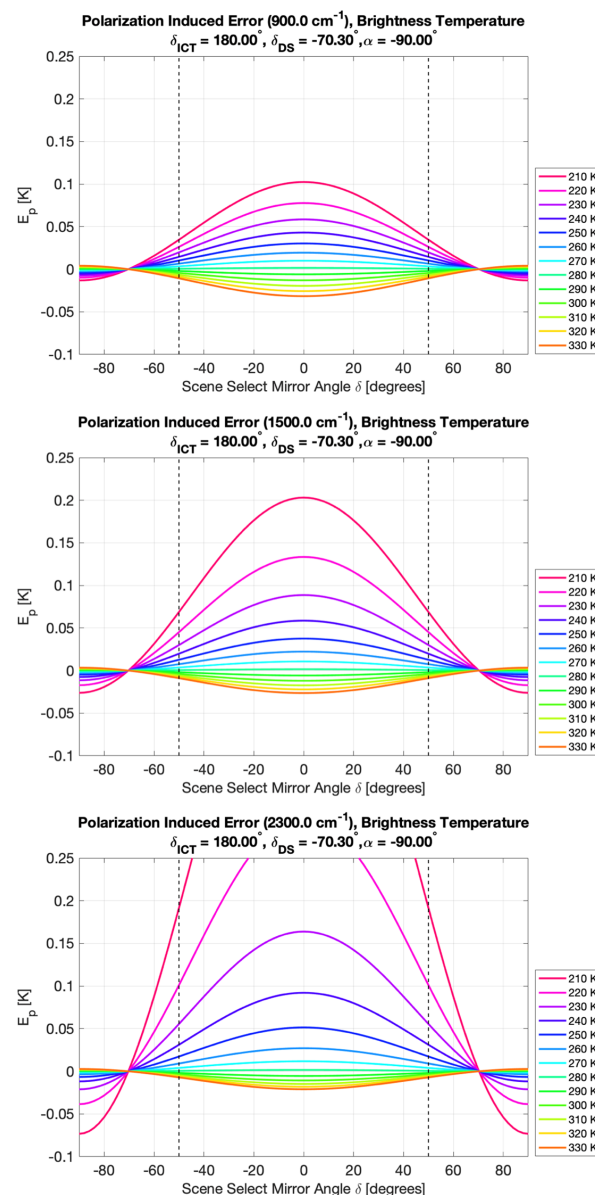


Figure 6. Modeled polarization-induced calibration error at 900 cm^{-1} (top panel), 1500 cm^{-1} (middle panel), and 2300 cm^{-1} (bottom panel) as a function of scene brightness temperature and scene select mirror angle. Constant values were used for the scene select mirror and instrument polarization ($p_r = 0.0055$, $p_t = 0.08$) and a sensor polarization angle of 0° was used for the preliminary model. The vertical dashed lines indicate the angular extent of the CrIS cross-track scan of the Earth.

4. The CrIS Polarization Parameters

There are several methods that can be used to determine the combined scene mirror and sensor polarization and sensor polarization angle for CrIS. Ideally, one would acquire CrIS calibrated radiance measurements of a fixed temperature, high accuracy blackbody source at a range of scene select mirror angles during thermal vacuum or bench testing. This radiance dataset and the expression for the calibration bias due to polarization (21) could be used to determine $p_r p_t$ and α for the CrIS sensor. The external blackbody temperature would need to be substantially hotter or colder than the scene select mirror temperature to achieve adequate signal to noise for resolving this small signal. As noted in the introduction, early analysis conducted prior to the test planning and launch of SNPP CrIS only included transmission effects and indicated that polarization induced calibration biases would not be significant enough to warrant characterization or a correction for CrIS. Accordingly, the bench and thermal vacuum test facility and test schedule were not configured to accommodate such a test. Subsequently, it was determined that adding such a procedure was not within the scope of the CrIS prelaunch test program and that the on-orbit pitch maneuver data and component level polarization measurements would be the best option for determining the polarization parameters. Component level polarization measurements were completed for the entire NOAA-20 (JPSS-1) CrIS optical chain and used to calculate the end-to-end perpendicular (S) and parallel (P) polarization state transmission of the sensor (interferometer, telescope, and aft-optics). While the component level measurements could be used in an instrument optical model to estimate the polarization correction parameters, the resulting estimates for $p_r p_t$ and α will depend both on the accuracy of the component level measurements and fidelity of the model, and will have a higher associated uncertainty than that for determining the parameters directly from the pitch maneuver data.

4.1. Pitch Maneuver Overview

A satellite pitch maneuver was conducted for both SNPP and NOAA-20 during the post-launch commissioning activities (20 February 2012 and 31 January 2018, respectively). The pitch maneuver, including a notional diagram illustrating the pitch maneuver for the SNPP satellite, is described in detail by Butler [18]. The pitch maneuver begins as the satellite enters the dark side of the orbit with a slight pitch forward of the spacecraft. The spacecraft then reverses from the forward dip into a backward pitch maneuver and is pitched completely away from viewing the Earth at approximately the midway point of the dark side of the orbit. At this point all the CrIS cross-track fields of regard that normally view the Earth are viewing deep space. The backward pitch maneuver continues throughout the dark side of the orbit, and the spacecraft returns to its nominal Earth viewing geometry before returning to the sunlit portion of the orbit. Roll, pitch, and yaw data from the NOAA-20 pitch maneuver are provided in Figure 7.

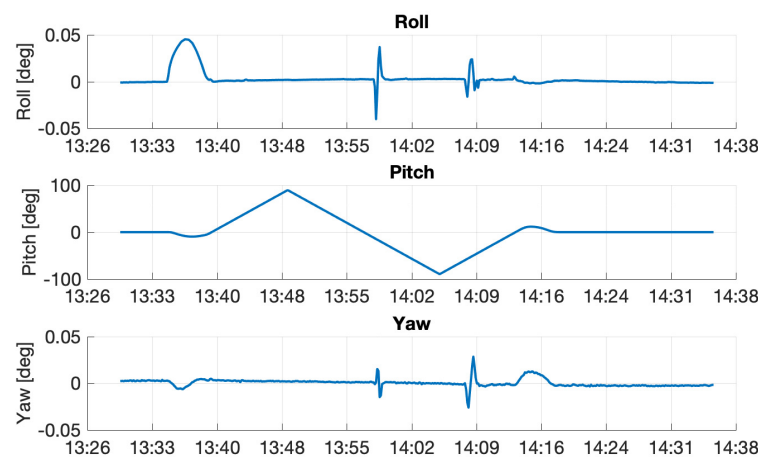


Figure 7. Roll, pitch, and yaw data for the NOAA-20 pitch maneuver.

During the pitch maneuver, all the CrIS cross-track fields of regard that normally view the Earth, view deep space. In this configuration, FOR and detector dependent differences are expected to be dominated by the instrument polarization, making this an ideal dataset for derivation of the polarization parameters directly from the CrIS calibrated radiances. This represents the only existing end-to-end measurements that can be used to derive the polarization parameters for CrIS.

4.2. Pitch Maneuver Dataset Description

As noted, the pitch maneuver is completed during the dark side of a single orbit, and there is only a short period of time in which all the CrIS cross-track fields of regard will be viewing deep space. The pitch data for NOAA-20 in Figure 7 shows that the entire maneuver is completed in approximately 45 min and it is evident from the radiance time series in Figure 8 and a radiance image in Figure 9 that all of the CrIS cross-track fields of regard view deep space for roughly 22 min during the 45-min maneuver.

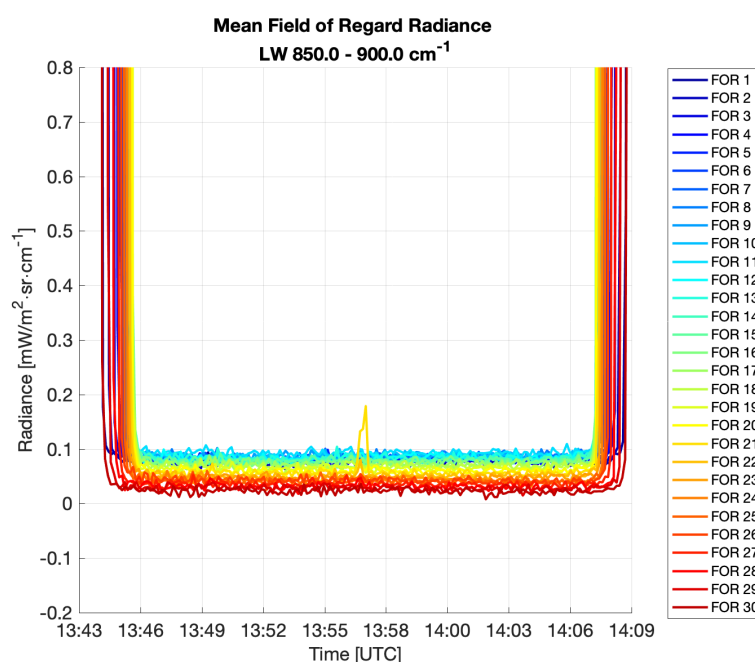


Figure 8. The NOAA-20 CrIS radiance time series for a spectral average from 850–900 cm^{-1} and averaged over all nine fields of view during the pitch maneuver.

The CrIS instrument uses a passive four-stage cooler, and during the pitch maneuver the instrument's Earth shields no longer block the Earth's radiation from the CrIS passive radiator and instrument. As a result, all four cooler stages rapidly warm during the maneuver as shown in Figure 10. This further reduces the time period for which the pitch maneuver data is nominal, especially for the longwave detector which has a responsivity and longwave cutoff that is more sensitive to these changes in detector temperature than that of the midwave and shortwave bands. With these considerations, approximately 4 min of longwave pitch maneuver data and 15 min of midwave and shortwave pitch maneuver data were selected for both the SNPP and NOAA-20 polarization parameter assessment. The primary considerations for data selection are rate of change of responsivity and instrument background and sufficient detector signal to noise ratio, which depend on detector and instrument temperature and rate of change of these temperatures. It was determined that after the first 4 min of valid pitch maneuver data for which all 30 cross-track fields of view had an unobstructed view of space, the rate of change in longwave band responsivity became large enough to impact the quality of the calibration. This is particularly problematic near the longwave cutoff of the longwave band as the location of the cutoff is quite sensitive to detector temperature. While these are very short datasets,

the excellent CrIS radiometric calibration accuracy and noise performance allows them not only to be sufficient, but invaluable for determining the polarization parameters.

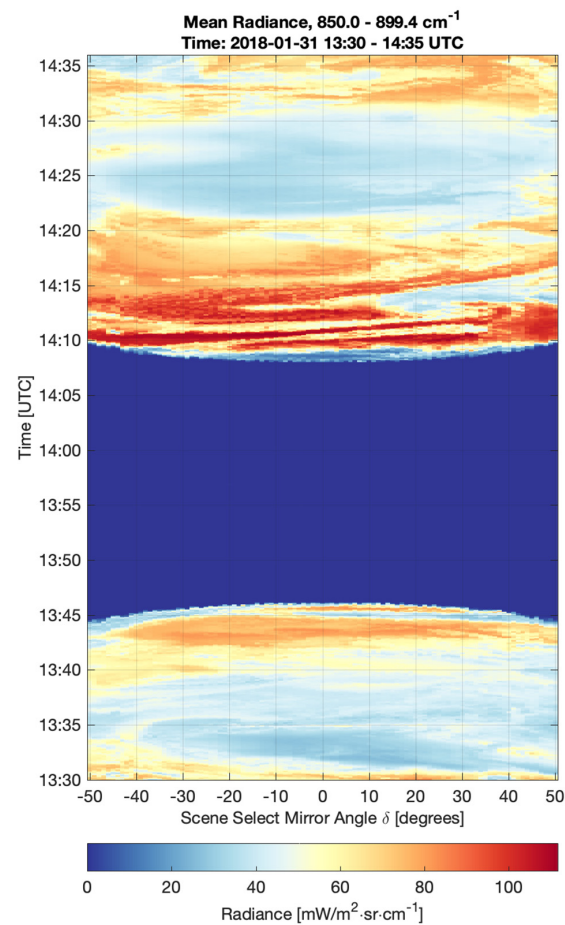


Figure 9. NOAA-20 CrIS radiance image. The CrIS calibrated radiance has been averaged from 850 to 900 cm^{-1} and plotted versus time (y-axis) and scene select mirror angle (x-axis). All cross-track fields of regard are viewing deep space between roughly 13:46 and 14:08 UTC.

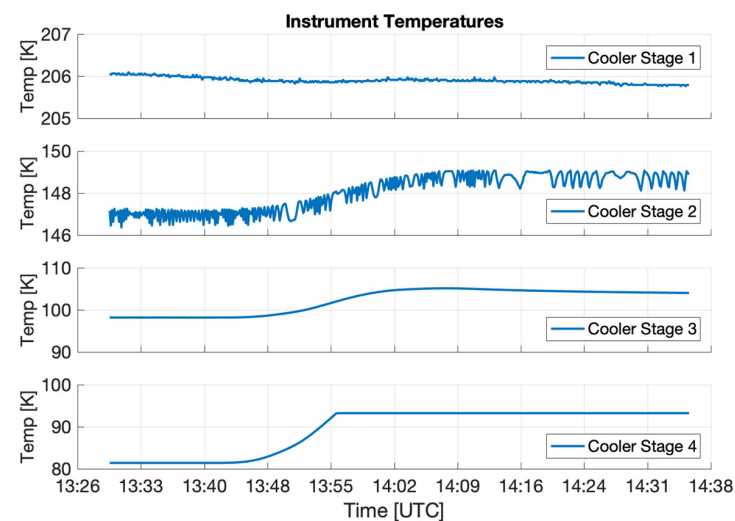


Figure 10. CrIS cooler stage temperatures during the pitch maneuver for NOAA-20. The maneuver began at approximately 13:34 UTC and ended at approximately 14:18 UTC. The cooler stage four temperature sensor was out of range shortly after 13:56 UTC.

4.3. Pitch Maneuver Analysis and Results

Analyses of the pitch maneuver data showed that the raw and calibrated signals exhibit clear polarization effects which were very well represented by the theoretical model. The calibrated radiances clearly exhibited the scene mirror angle dependence described by Equation (21) and the raw spectra demonstrated a sinusoidal modulation dependence on scene select mirror angle δ with four zero crossings in 360° , as predicted by the linear polarizer-analyzer pair model presented in Section 2.2. A NOAA-20 radiance image for the region of the pitch maneuver where all the CrIS cross-track fields of regard are viewing deep space is shown in Figure 11. The radiance data in the image has been spectrally averaged over $850\text{--}900\text{ cm}^{-1}$ and the nine longwave (LW) detector fields of view have been averaged for each FOR. The resulting data is plotted versus time and scene select mirror angle. Since all fields of regard are viewing deep space for this data, there should be no dependence of the calibrated radiance on FOR. However, a clear dependence on FOR is evident, with the warmest radiance at a scene select mirror angle of approximately $\delta = 15^\circ$. Since the dependence of the radiance bias on scene mirror angle is not symmetric about $\delta = 0^\circ$ for the longwave, it is clear from the image that the interferometer beamsplitter and the refractive aft optics (including dichroics) both contribute significantly to the effective sensor polarization angle for the longwave band. Details of the analysis and the results for all three bands will be discussed in this section.

The nominal CrIS calibration algorithm was modified slightly to optimize signal to noise and accurately calibrate the pitch maneuver data. The CrIS scene select mirror is used to direct either scene or calibration reference radiance into the CrIS sensor. The CrIS instrument collects deep space and ICT calibration reference views for every cross-track scan, for both the forward and reverse interferometer sweep directions. A typical measurement scan sequence consists of 34 interferogram collections (alternating forward and reverse interferometer sweep direction) and consists of 30 Earth scenes, two deep space, and two ICT measurements. One measurement scan sequence of the CrIS sensor takes roughly 8 s to complete. A diagram illustrating the CrIS 8-s scan sequence is provided in Figure 12.

An interferometer sweep direction dependent moving average is applied to the calibration reference views during the CrIS processing. The moving average window is typically 29 scan lines wide (in the NASA L1b processing), such that it includes the calibration reference data for the 14 measurement scan sequences prior to and after the current scene select mirror measurement scan sequence. Since the instrument temperatures are changing more rapidly during the pitch maneuver the moving average window width was reduced to 9 scan lines (current measurement scan line ± 4 scan lines). This results in increased noise due to fewer measurements in each average but accommodates the atypical rates of change of instrument temperature and the small dataset period. The component level polarization measurements indicated that the spectral dependence of the CrIS combined scene mirror and sensor polarization had a low frequency spectral dependence in all detector bands with no high spectral resolution features. Therefore, the pitch maneuver data was processed at a lower spectral resolution to improve signal to noise. Several processing options were tested, and it was determined that processing the pitch maneuver data at an apodized resolution of 2.5 cm^{-1} provided excellent signal to noise performance while retaining sufficient spectral resolution to resolve the spectral dependence of $p_r p_t$. The results were compared to the normal spectral resolution (NSR) processing to confirm that no additional artifacts were introduced by this calibration modification.

Since the CrIS instrument is operating in a non-nominal orientation for the pitch maneuver, one of the most important aspects of the analyses is inspection and quality control of the data. As noted earlier, the CrIS radiometric calibration utilizes the Revercomb complex calibration method [14]. Complex calibration operates on the complex valued spectra and is an efficient method developed to correct the amplitude and phase of the measured spectrum. For this method, successful calibration of good quality data will result in an imaginary component of the calibrated radiance that is predominantly noise. Accordingly,

the imaginary component of the calibrated radiance along with the sensor temperature and telemetry values were used to assess the data quality for the pitch maneuver data and omit questionable data from the analysis. An example of spurious data that was omitted from the dataset is evident in Figures 8 and 11. An outlier in the calibrated radiance is evident at approximately 13:57 UTC for FOR 21. This effect is also obvious in the imaginary part of the calibrated radiance, and a spike in roll and yaw data is also observed at this time (Figure 7). A conservative approach for quality control was utilized, and other outliers for which the impact on the calibrated radiance was not obvious but still detectable in the imaginary part of the calibrated radiance were also flagged as questionable and omitted from the polarization parameter analysis.

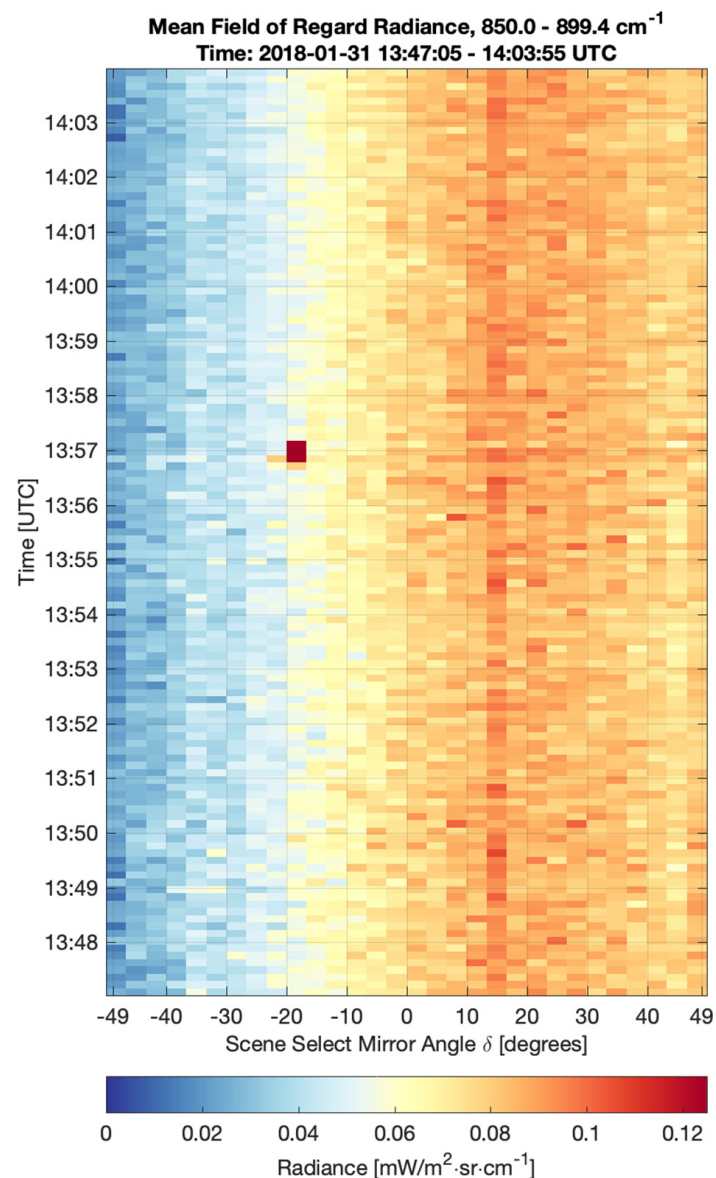


Figure 11. NOAA-20 CrIS radiance image, spectrally averaged from 850–900 cm^{-1} , and averaged over all fields of view during the pitch maneuver, plotted versus time (y-axis) and scene select mirror angle (x-axis). An outlier in the calibrated radiance is evident at approximately 13:57 UTC for FOR 21 (at approximately -20° SSM angle). This effect is also obvious in the imaginary part of the calibrated radiance, and a spike in roll and yaw data is also observed at this time (Figure 7). One of the most important aspects of the analyses is inspection and quality control of the data such that outliers such as this do not impact the analysis.

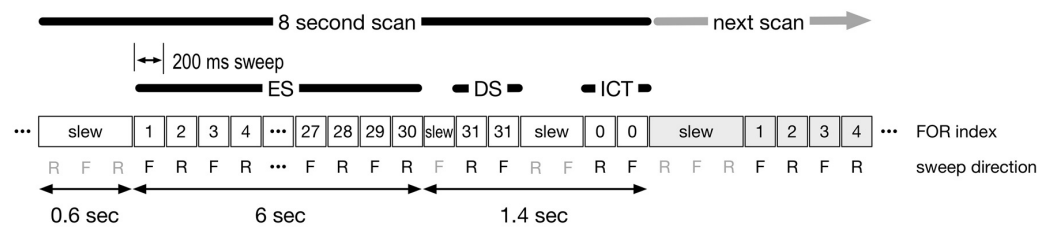


Figure 12. CrIS 8-s measurement scan sequence. The interferometer sweep directions are denoted as ‘F’ for forward and ‘R’ for reverse. The 200-millisecond interferometer sweep time includes turnaround at end of scan.

The determination of the polarization parameters from the pitch maneuver data was conducted in two main steps and the same analysis was applied to both sensors. As noted earlier, 4 min of longwave pitch maneuver data and 15 min of midwave and shortwave pitch maneuver data were selected for both the SNPP and NOAA-20 polarization parameter assessment.

The first step of the pitch maneuver analysis utilizes uncalibrated magnitude spectra to independently determine the sensor polarization angle α for all detectors in the longwave, midwave, and shortwave bands. The forward and reverse interferometer sweep direction data were analyzed independently for this step of the analysis since it is conducted on the uncalibrated spectra and not the calibrated radiances.

Sinusoidal modulation of the band averaged magnitude spectra versus $(\delta - \alpha)$ was evident for all three bands of both SNPP and NOAA-20, and an example for the NOAA-20 longwave band is presented here. The signal to noise of the observed modulation signature was best for the longwave band and lowest for the shortwave band for both SNPP and NOAA-20, despite the short four-minute analysis period for the longwave band due to detector temperature considerations.

Plots of the longwave band average ($650\text{--}1095\text{ cm}^{-1}$) raw magnitude spectra as a function of scene mirror angle are shown for the nine NOAA-20 longwave detectors in Figure 13. The blue dots represent the mean over the analysis period for the normally Earth observing cross-track fields of regard, the red dots are the mean for the deep space view, and the smaller grey markers correspond to the individual band averaged measurements. Only the even numbered cross-track fields of regard and the deep space view with the same interferometer sweep direction are shown in this figure but the same behavior was also observed for the opposite interferometer sweep direction.

Equation (12) predicts that the raw signal modulation due to polarization should be sinusoidal with a period of 180° . Accordingly, a sinusoid with modulation amplitude A and y -offset y_0 , as described by Equation (22) was fit to the data to determine α for each detector.

$$y = A \cdot \cos 2(\delta - \alpha) + y_0 \tag{22}$$

The resulting sinusoidal fit is indicated by the orange solid line in Figure 13. The y -offset y_0 has been removed from both the data and sinusoidal fit for each subplot in Figure 13 but is noted in the title of each subplot. The y -offset ranges from approximately 23,000 to 56,000 analog-to-digital (ADC) counts for the NOAA-20 longwave pitch maneuver data shown in the example provided figure, and the large range is due to the different responsivities and PGA gains for each detector. To appreciate the small size of the modulated signal, consider that the corresponding modulation amplitude is less than 80 ADC counts for all NOAA-20 LW FOVs, which corresponds to approximately 0.2% of the unmodulated signal. The band averaged longwave magnitude spectra in Figure 13 show a clear sinusoidal dependence that is fit well by the model. A small FOV dependence of α is evident and as noted in Section 3 is expected to be due to the small differences in optical paths and angles of incidence at optical elements for the 9 FOVs, particularly in the aft optics.

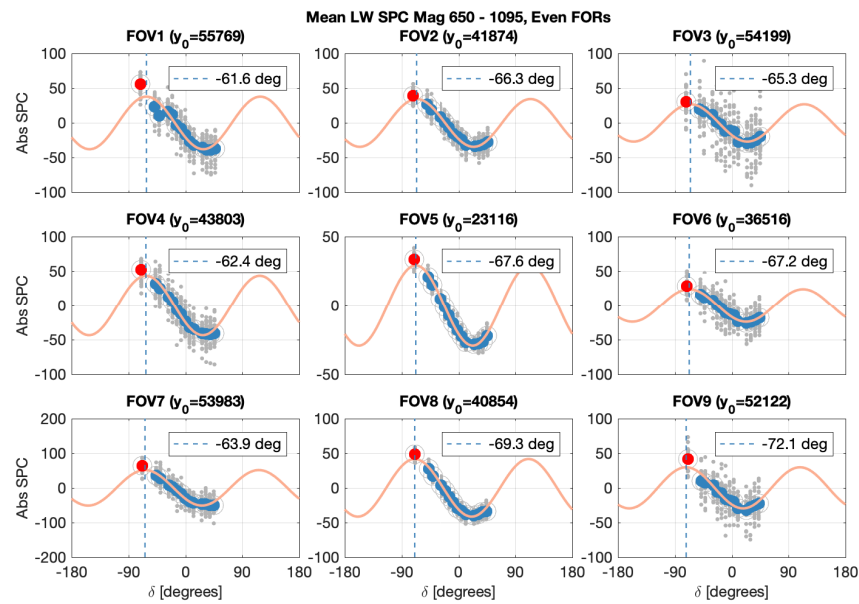


Figure 13. Longwave band average of NOAA-20 magnitude spectra during the pitch maneuver. The blue dots represent the mean over the analysis period for the normally Earth observing cross-track fields of regard, the red dots are the mean for the deep space view, and the smaller grey markers correspond to the individual band-averaged measurements. Only the even-numbered cross-track fields of regard and the deep space view with the same interferometer sweep direction are shown in this figure but the same behavior was also observed for the opposite interferometer sweep direction.

The sensor polarization angle values derived from the uncalibrated magnitude band averaged spectra in the first step of the analysis were used as the first guess and to establish localization constraints for α in the second step of the polarization parameter identification. During the second step of the analysis, $p_r p_t$ and α are derived simultaneously via a nonlinear least squares fit of the predicted calibration bias due to polarization (E_p^δ) as described by Equation (21) to the pitch maneuver calibrated radiances. The cost function (E) used in the nonlinear least squares fit is defined as

$$E = (L_{\delta,S} - L(T_{DS})) - E_p^\delta$$

In the cost function, $L_{\delta,S}$ are the CrIS calibrated radiances of deep space for all 30 cross-track fields of view, affected by the calibration bias due to polarization; and $L(T_{DS})$ is the predicted Planck radiance for deep space.

The results for SNPP and NOAA-20 are summarized in Figure 14 (longwave), Figure 15 (midwave), and Figure 16 (shortwave). In these figures, SNPP is shown in red and NOAA-20 is shown in black, and the lighter weight lines indicate the $p_r p_t$ results corresponding to application of the same analysis to the calibrated radiances averaged over all fields of view with no noise filtering or spectral conditioning applied to the resulting FOV averaged $p_r p_t$. The all-FOV average agrees well with the center FOV 5 result, which is reasonable since the all-FOV calibrated radiance average effectively has the same mean optical path through the sensor as FOV 5. As expected, the effective polarizer angle of the sensor has detector band and a small FOV dependence and the combined polarization ($p_r p_t$) of the SSM and sensor is wavenumber dependent and has a small FOV dependence. SNPP CrIS and NOAA-20 CrIS exhibit small differences in their pitch maneuver derived polarization parameters, which is likely due to optical coating differences between the two instruments.

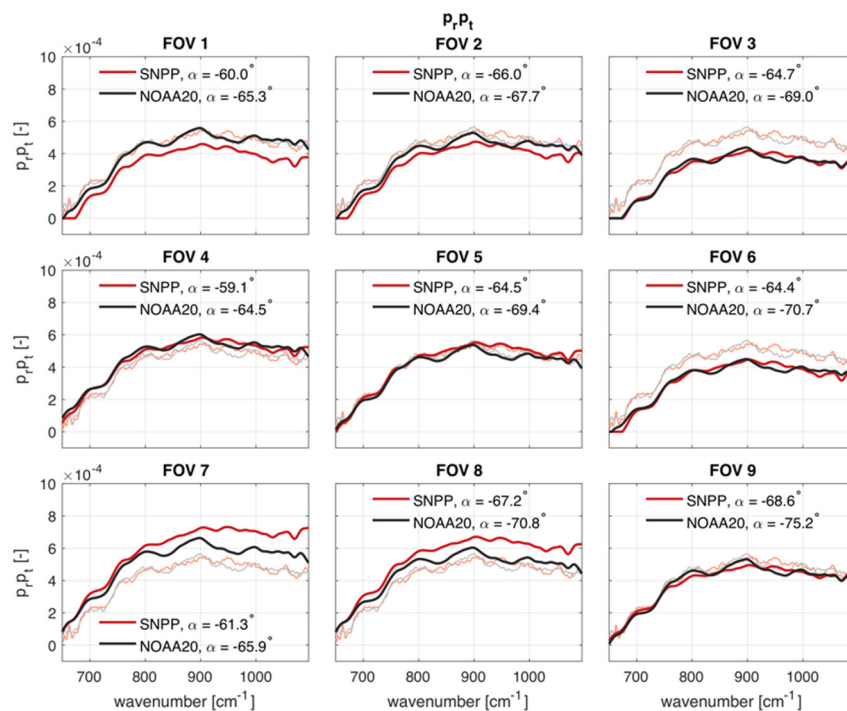


Figure 14. Combined scene select mirror and sensor polarization ($p_r p_t$) and sensor polarization angle derived from the longwave pitch maneuver data. SNPP is shown in red, and NOAA-20 is shown in black. The lighter weight lines are the derived $p_r p_t$ values for the average over all nine detectors, with no noise filtering or spectral averaging applied.

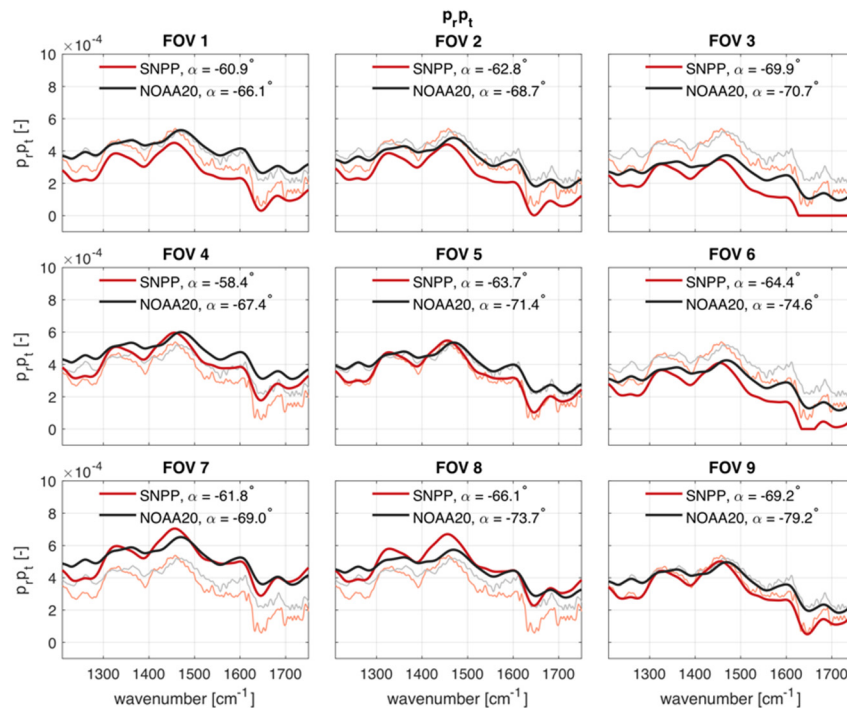


Figure 15. Combined scene select mirror and sensor polarization ($p_r p_t$) and sensor polarization angle derived from the midwave pitch maneuver data. SNPP is shown in red, and NOAA-20 is shown in black. The lighter weight lines are the derived $p_r p_t$ values for the average over all fields of view, with no noise filtering or spectral averaging applied.

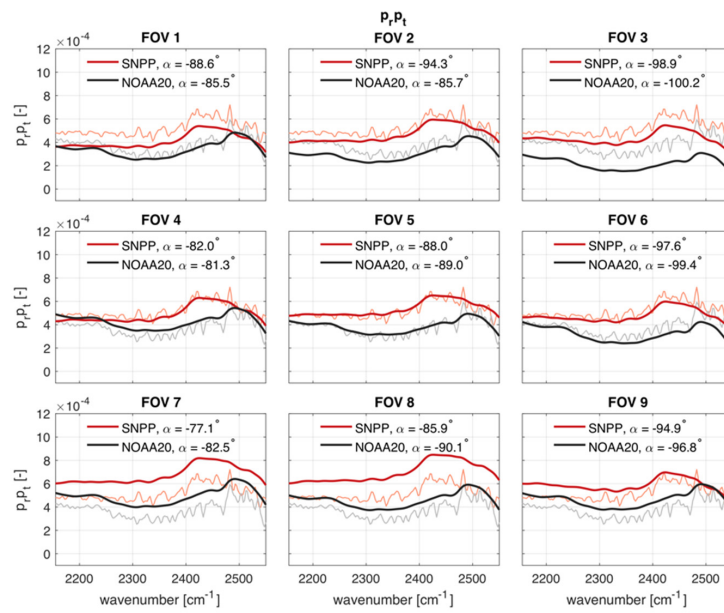


Figure 16. Combined scene select mirror and sensor polarization ($p_r p_t$) and sensor polarization angle derived from the shortwave pitch maneuver data. SNPP is shown in red, and NOAA-20 is shown in black. The lighter weight lines are the derived $p_r p_t$ values for the average over all fields of view, with no noise filtering or spectral averaging applied.

5. Correction of Earth Scene Radiances for Radiometric Modulation due to Polarization

This section provides example results for the correction of view angle dependent radiometric biases due to polarization for the CrIS instrument that illustrate the sensor, FOV, FOR, spectral, and scene dependence of the polarization correction and updates the radiometric uncertainty estimate to include the contribution associated with the uncertainty in polarization correction. Polarization correction is included in the CrIS NASA L1b Version 3 product and in the NOAA IDPS Block 2.1 Mx8 processing. Both calibration packages use the same polarization parameters and correction algorithm, and the polarization correction has been confirmed as consistent between the two products. The results presented in this section were generated the CrIS NASA L1b Version 3 software. The relationship between the correct calibrated radiance L_S and the calibrated radiance affected by the calibration bias due to polarization $L_{\delta,S}$ was provided by Equation (19), and is reproduced here for convenience:

$$L_S = L_{\delta,S} - E_p^\delta$$

Recall, we have defined the polarization correction as $-E_p^\delta$, equal in magnitude and opposite in sign of the calibration bias due to polarization.

5.1. FOR and Scene Temperature Dependence of the Polarization Correction

The calculated polarization correction ($-E_p^\delta$) at 900 cm^{-1} , 1500 cm^{-1} , and 2300 cm^{-1} versus scene select mirror angle is shown in Figure 17. The NOAA-20 pitch maneuver derived parameters have been used in the calculation. The vertical dashed lines in the figure indicate the extent of the CrIS Earth scene fields of regard, with the centers of FOR 1 and 30 at scene select mirror angles of approximately 48.33° and -48.33° , respectively. The SSM angle (FOR) dependence of the correction is clear in Figure 17, with the largest correction at an SSM angle of approximately $+20^\circ$ from nadir in the longwave and midwave bands, and at nadir in the shortwave band. The correction is symmetric with respect to the peak correction angle. The dependence on scene temperature is also evident, with the size of the correction increasing with difference between the scene temperature and SSM temperature, and the largest correction corresponding to the coldest scene temperatures. Comparing the magnitude of the polarization correction using the NOAA-20 polarization parameters shown

in Figure 17 to the modelled polarization induced calibration error using preliminary values (Figure 6), it is evident that the impact of polarization on NOAA-20 CrIS is slightly larger in the longwave band, and slightly smaller in the midwave and shortwave bands than the preliminary model, at the wavenumbers plotted. Most notable are the differences in the sensor polarization angle for the longwave and midwave bands, for which the preliminary model ignored the contribution of the aft-optic dichroics. This results in a shift of the SSM angle for which the peak polarization induced error occurs in the longwave and midwave bands (approximately $+20^\circ$ versus 0° in the preliminary model). As noted earlier, with the polarization correction expressed in equivalent brightness temperature, the size of the correction also increases with wavenumber with the largest correction at the coldest scenes and shortest wavelengths. This dependence on wavelength is largely due to the nature of the Planck function and the nonlinear relationship between radiance and brightness temperature, with small changes in radiance resulting in large changes in brightness temperature for cold scenes and short wavelengths.

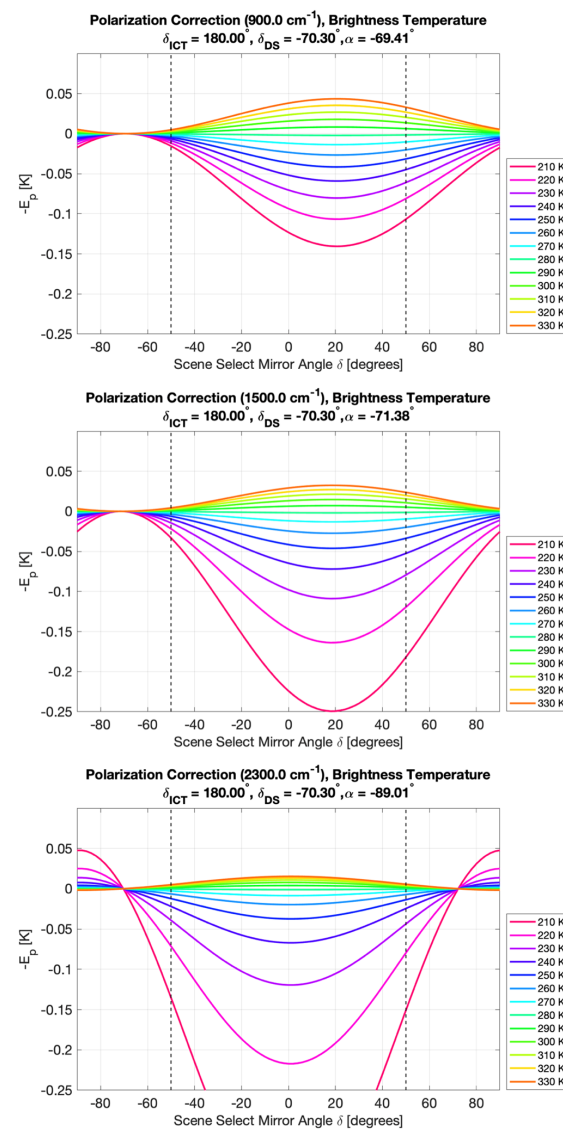


Figure 17. Calculated polarization correction at 900 cm^{-1} (top panel), 1500 cm^{-1} (middle panel), 2300 cm^{-1} (bottom panel) as a function of scene brightness temperature and scene select mirror angle. The NOAA-20 CrIS pitch maneuver derived values have been used for the scene select mirror and instrument polarization and sensor polarization angle. The vertical dashed lines indicate the angular extent of the CrIS cross-track scan of the Earth.

5.2. FOV and Sensor Dependence of the Polarization Correction

As discussed in Section 4, the polarization parameters (p_r, p_t, α) derived from the pitch maneuver data exhibited a small FOV dependence as well as sensor to sensor differences both of which were expected and reasonable. In this section, the impact of the polarization parameter sensor and FOV differences on the polarization correction ($-E_p^\delta$) are illustrated. The polarization correction is calculated for two scene radiance examples: a tropical scene over warm ocean and an Antarctic scene. In each case, a common radiance is used for all fields of view for both sensors, and the differences in the polarization correction are due to the FOV and sensor dependence of the polarization parameters. The example tropical scene results are provided in Figure 18 and the Antarctic scene results are provided in Figure 19. The scene radiance and polarization correction have been Hamming apodized and converted from radiance to brightness temperature in these figures. When expressed in brightness temperature units, the magnitude of the correction and the FOV and sensor dependence is largest for short wavelengths and cold scenes. The polarization correction plotted in these figures represents the average over all thirty Earth scene fields of regard.

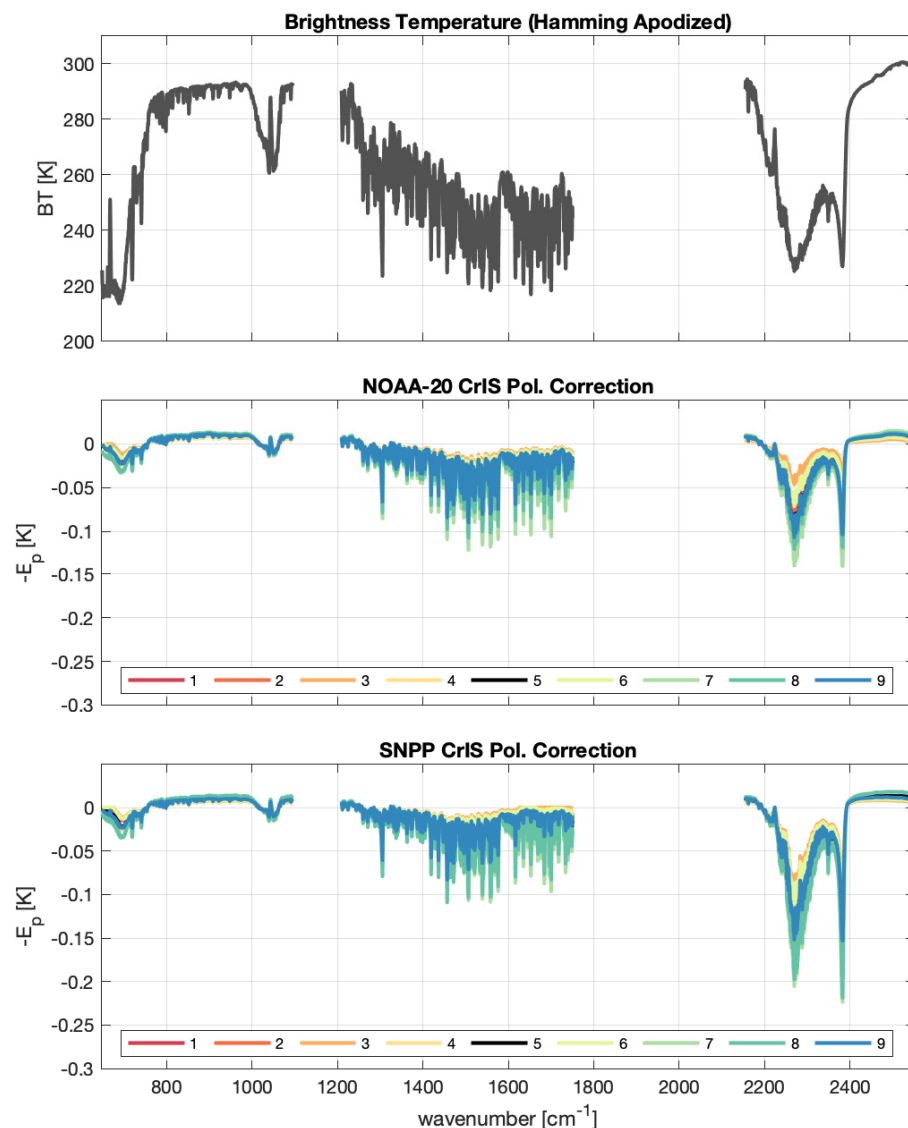


Figure 18. FOV and sensor dependence of the polarization correction for an example of a tropical atmosphere over ocean.

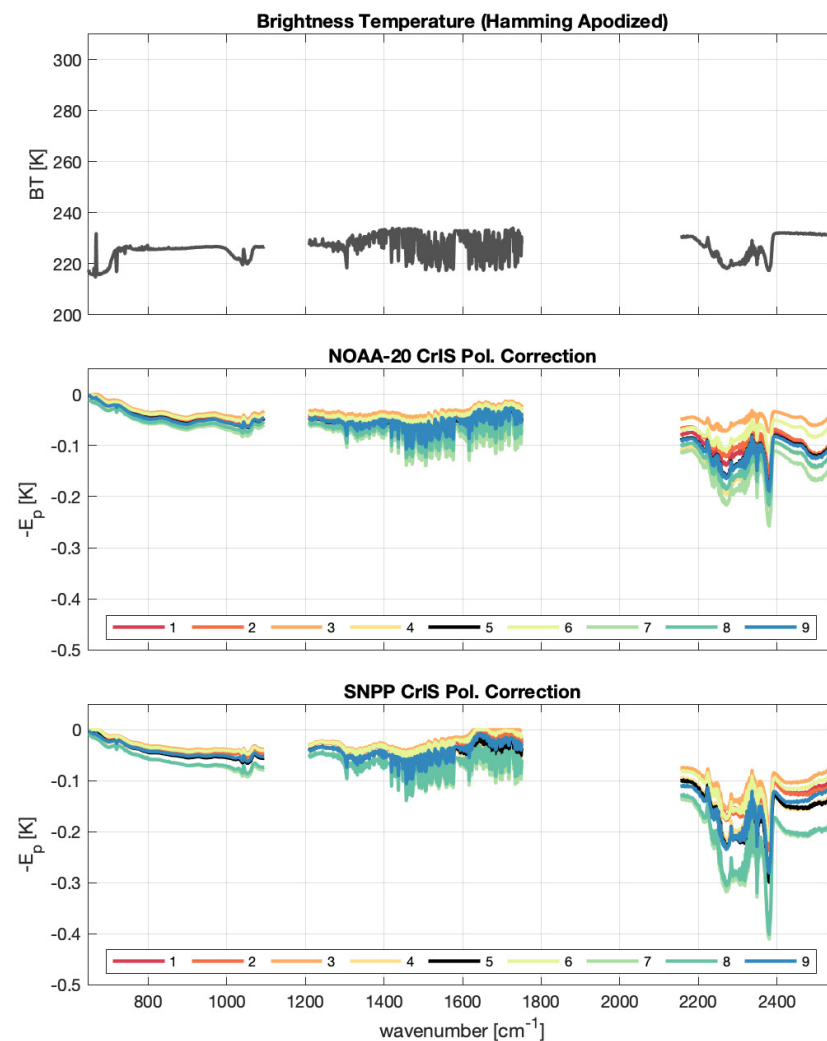


Figure 19. FOV and sensor dependence of the polarization correction for an example of an Antarctic observation.

The polarization correction and FOV dependence of the polarization correction is very similar between the SNPP and NOAA-20 CrIS sensors in the longwave for the tropical ocean scene with less than 0.025 K difference in the correction across all nine detectors for each sensor. The differences between the two sensors are more evident for the extremely cold Antarctic scene in the longwave, but still quite small with a maximum correction of approximately -0.09 K for SNPP and 0.075 K for NOAA-20. Like the longwave band, the midwave polarization correction and FOV dependence is similar between the two sensors for the tropical ocean scene, with the FOV and sensor differences becoming more noticeable, but still small, for the cold Antarctic scene. The most noticeable FOV and sensor dependence is evident in the shortwave band. It is clear in Figure 16 that the combined SSM and sensor polarization in the shortwave band is larger for SNPP than NOAA-20, and this has a noticeable impact on the magnitude of the polarization correction for SNPP in comparison with NOAA-20 for both the tropical and Antarctic scenes. In the shortwave, both sensors exhibit a more significant FOV dependence in their respective polarization corrections, when expressed in brightness temperature. Again, it is important to note that due to the nature of the Planck function and conversion from radiance to brightness temperature via inversion of the Planck function, a very small change in radiance for shorter wavelengths and cold scenes corresponds to a large brightness temperature difference.

5.3. Polarization Correction Results: Global Coverage

While the preceding section used two scene radiance examples to characterize FOV and sensor dependencies, it is useful to examine a larger set of data to further illustrate the nature and statistics of the polarization correction. This section utilizes 12 consecutive hours of NOAA-20 data, providing global coverage in a combination of ascending and descending orbits (1 April 2018, 00:06–12:06 UTC). A global map showing the shortwave band average brightness temperature for this 12-h dataset is shown in the top panel of Figure 20 and the corresponding band average polarization correction $\langle -E_p^\delta \rangle_{SW}$ is shown in the bottom panel of the same figure. The global brightness temperature maps clearly confirm that the largest polarization corrections correspond to the coldest scenes, which for this 12-h dataset have shortwave band average temperatures as cold as ~230 K and a corresponding band averaged polarization correction as large as ~0.18 K.

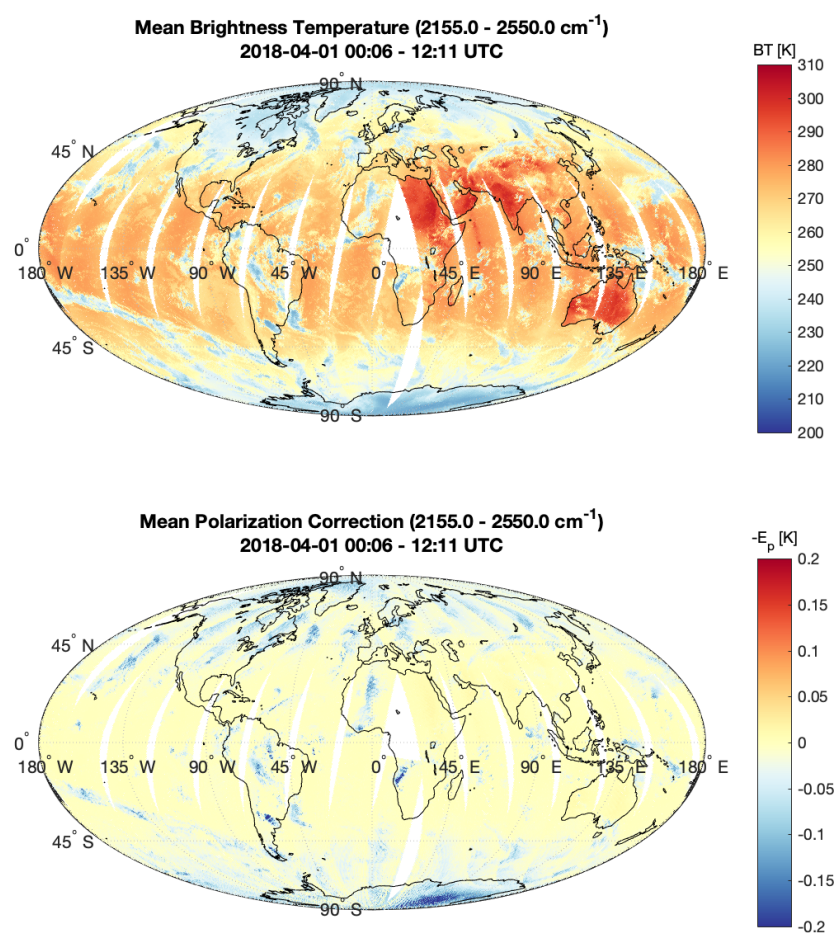


Figure 20. NOAA-20 CrIS shortwave band-averaged brightness temperature map (top panel) and corresponding band-averaged polarization correction for 12 h of data on 1 April 2018 (00:06–12:11 UTC).

The spectral dependence of the correction for the 12-h dataset is shown in Figure 21 for all three bands for scene brightness temperatures between 200 K and 320 K. The mean and range of the scene brightness temperature for all fields of view and fields of regard and the corresponding polarization correction are provided in the top and middle rows of the figure, respectively. Distribution density plots of the polarization correction versus scene temperature for the longwave (left), midwave (center), and shortwave (right) are shown in the bottom row of Figure 21. The distributions are plotted on a logarithm color scale and include values from all spectral channels, fields of view, and fields of regard within each band.

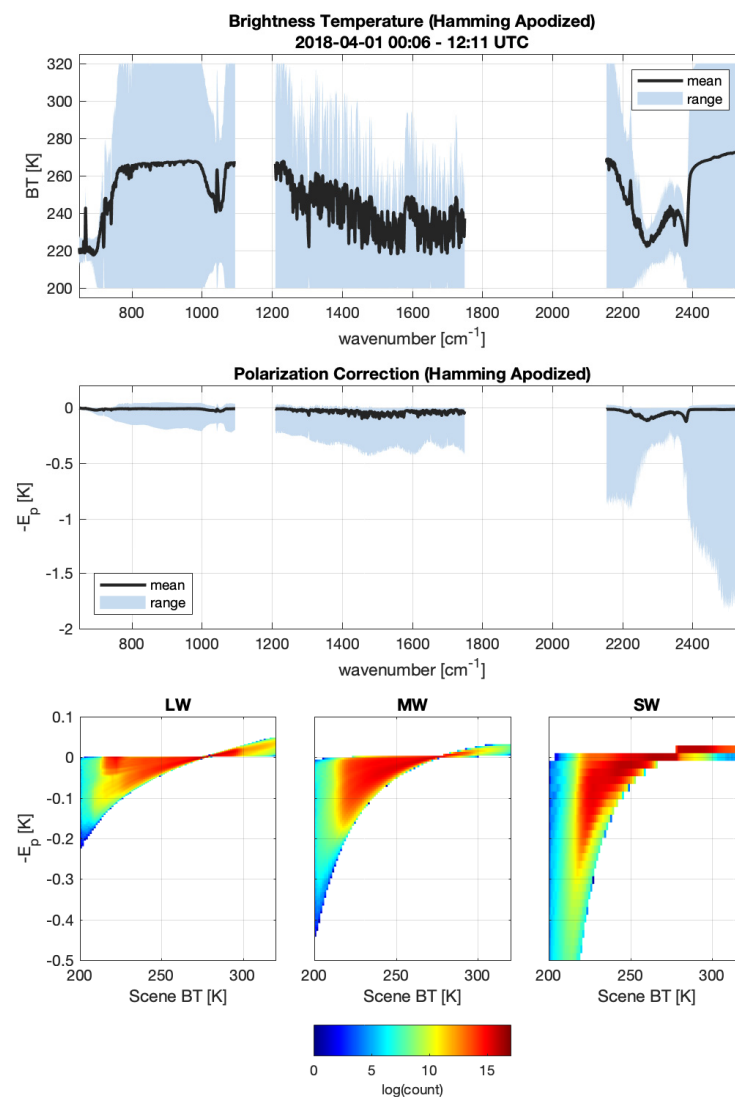


Figure 21. NOAA-20 polarization correction as a function of scene brightness temperature for scene brightness temperatures between 200 K and 320 K for 12 h of data on 1 April 2018 (00:06–12:11 UTC). The spectrally resolved scene brightness temperatures (mean and range) are shown in the top panel and the corresponding polarization corrections (mean and range) are provided in the middle panel. The distribution of polarization correction versus scene brightness temperature for the longwave (left), midwave (center), and shortwave (right) are shown in the bottom panel.

5.4. Estimated Radiometric Uncertainty Associated with Correction

As noted in the introduction, early polarization analysis of SNPP CrIS only considered transmission effects and as a result, polarization was not expected to be a significant contributor to any calibration bias or radiometric uncertainty and was not included in the original calibration algorithm or in the SNPP RU assessment by Tobin et al. [7]. The total radiometric uncertainty, without considering polarization effects is shown in Figure 1 for SNPP and NOAA-20 CrIS. Figures 22 and 23, show the on-orbit 3- σ radiometric uncertainty estimate for one orbit of data from the SNPP and NOAA-20 CrIS sensors, respectively. In these figures, the RU is shown as a density plot of radiometric uncertainty in brightness temperature versus scene brightness temperature for all spectral channels, fields of view, and fields of regard. In both figures, the longwave band results are in the left column, the midwave results in the middle column, and the shortwave results in the right column. The top row of each plot provides the radiometric uncertainty if no polarization correction is applied, and the full polarization correction is included in the radiometric uncertainty

estimate. The middle row presents the radiometric uncertainty in the CrIS NASA L1b Version 3 and NOAA IDPS Block 2.1 Mx8 (and subsequent versions of each product). In this case, the polarization correction is included in the calibration algorithm, with a $3\text{-}\sigma$ uncertainty in the combined scene select mirror and sensor polarization ($p_r p_t$) of 20%, and the $3\text{-}\sigma$ uncertainty in the sensor polarization angle (α) of 10° . These are conservative estimates of the uncertainty, based on the analysis and derivation of the parameters from the pitch maneuver data. The estimation of the uncertainty in the polarization parameters includes consideration of (1) the noise in the pitch maneuver data used for the polarization parameter determination, (2) the impact on calibration accuracy due to the transient thermal conditions during the pitch maneuver, (3) the small range of sensor polarization angles determined for the spectral channels within each band, (4) and margin for any change in parameters associated with potential changes in optical coatings during the on-orbit lifetime of the sensor. Ideally, an end-of-life pitch maneuver would be completed during sensor decommissioning to quantify any changes in polarization parameters on-orbit and refine the uncertainty estimates. The bottom row in Figures 22 and 23 indicate the total radiometric uncertainty if the CrIS sensor had zero polarization sensitivity and is consistent with Figure 1.

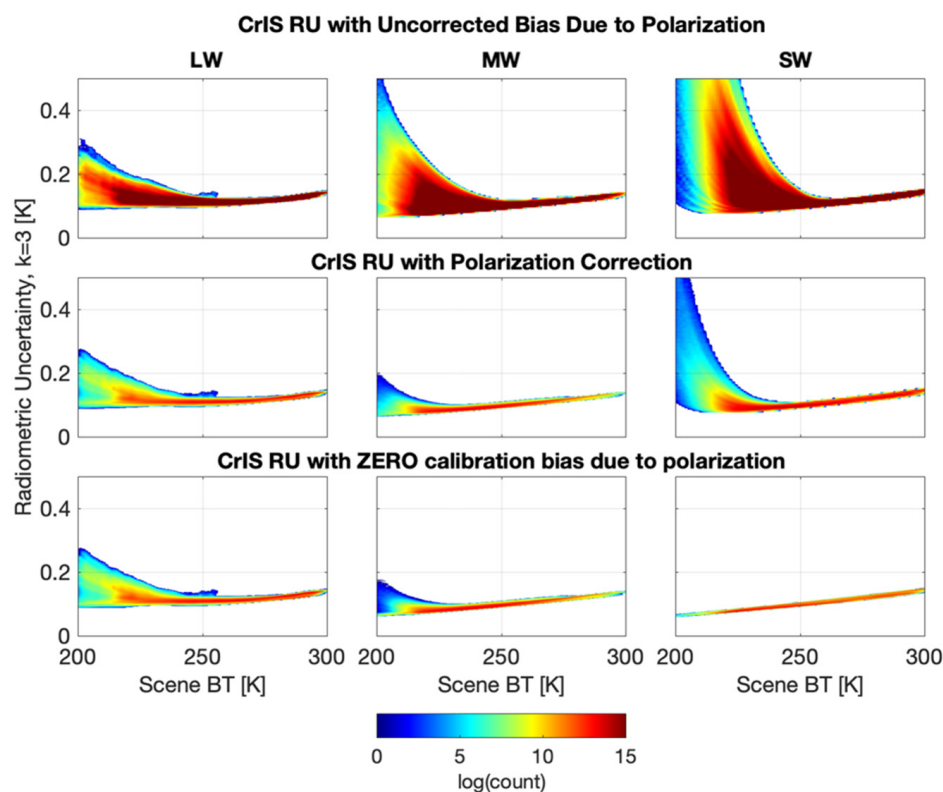


Figure 22. On-orbit $3\text{-}\sigma$ ($k = 3$) radiometric uncertainty estimate for one orbit of data from SNPP CrIS. The RU is shown as a density plot of brightness temperature uncertainty versus scene brightness temperature for all spectral channels, fields of view, and fields of regard. The longwave band results are in the left column, the midwave results are in the middle column, and the shortwave results are in the right column. Top row: no polarization correction is included in calibration, and the full polarization error is included in the RU estimate; middle row: polarization correction is applied in the calibration, and the uncertainty contribution of the polarization correction is included in total RU estimate; bottom row: total RU if the sensor had zero polarization sensitivity (consistent with Figure 1).

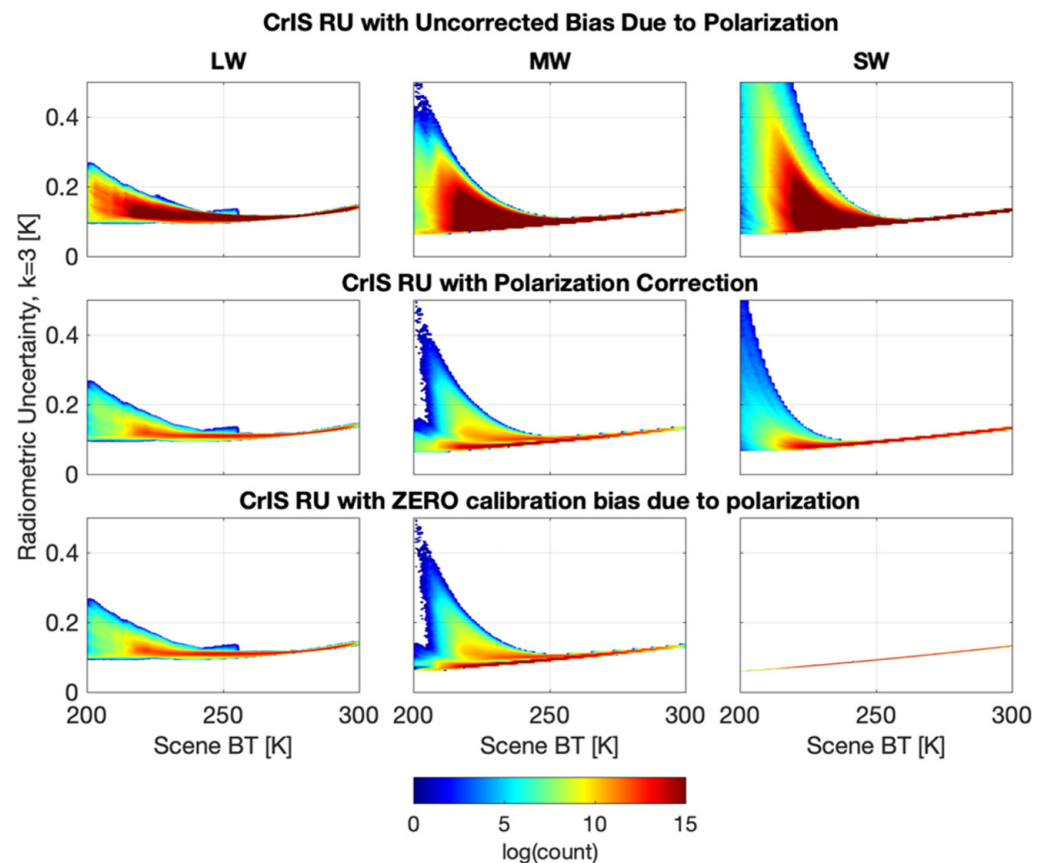


Figure 23. On-orbit $3\text{-}\sigma$ ($k = 3$) radiometric uncertainty estimate for one orbit of data from NOAA-20 CrIS, presented in the same format as Figure 22.

Analyses have shown that the primary contributors to the CrIS radiometric uncertainty are the individual uncertainties in

1. The Internal Calibration Target (ICT) temperature, ICT effective cavity emissivity, and the temperatures of the reflected terms in the ICT environmental model,
2. The quadratic coefficient in the nonlinearity correction,
3. The polarization correction parameters (combined scene mirror and sensor polarization and the sensor polarization angle).

The CrIS shortwave band has no detectable nonlinear response, and no RU contribution from nonlinearity correction. Thus, the primary RU contributors for the shortwave band are the predicted ICT radiance uncertainty and polarization correction uncertainty. Therefore, the RU due only to uncertainties in the predicted ICT radiance (primarily ICT temperature uncertainty) is illustrated for the shortwave in the bottom right panel of Figures 22 and 23, for the case of a CrIS sensor with zero radiometric bias and no RU contribution due to polarization. The RU contribution from uncertainties in the predicted ICT radiance has a similar dependence on scene temperature in the longwave and midwave bands and a consistent contribution to the overall RU in all bands. All longwave and midwave detectors in SNPP CrIS, and all longwave and one midwave detector in NOAA-20 CrIS have nonlinear responses that are large enough to require correction, and the uncertainty in the nonlinearity correction for these detectors also has a noticeable contribution to the total radiometric uncertainty. For Earth scenes, the nonlinearity corrections and resulting RU contributions are dependent on the spectrally integrated signal, as well as the spectral shape of the Earth view spectra, and thus can vary significantly from one spectrum to another. This effect is evident in the longwave and midwave RU density plots provided in Figures 1, 22 and 23. In each of these figures, observations from all spectral channels (with the band), all fields of view, and all fields of regard are combined in each

panel, which results in a range of radiometric uncertainties for a given scene temperature that is noticeable for scene temperatures less than ~ 260 K in the plots. Furthermore, as noted in the introduction, two distributions are also evident in the NOAA-20 midwave RU, one having larger RU (associated with midwave FOV 9 which has an anomalously large nonlinear response), and one that is quite similar in shape and magnitude to the SNPP midwave RU distribution. Since the polarization correction has a wavenumber and view angle dependence, there is also a range of radiometric uncertainties associated with the polarization correction for a given scene temperature. It is clear from the top row Figures 22 and 23 that the magnitude of the radiometric bias due to polarization is larger than the total radiometric uncertainty due to all other contributors in parts of the midwave and shortwave bands for cold scenes when left uncorrected. A comparison of the second and third rows in Figures 22 and 23 shows that when a polarization correction is included in the calibration, the radiometric uncertainty due to polarization is a negligible contributor to total radiometric uncertainty for the longwave band, a small contributor in the midwave band, and the dominant contributor in the shortwave band for cold Earth scenes (below ~ 240 K).

6. Impact on Inter-Instrument Comparisons

The impact of the polarization correction on a comparison of each SNPP and NOAA-20 CrIS with METOP-B IASI is shown in Figure 24. This result uses simultaneous nadir overpasses over a three-month time period from November 2018 through January 2019 and focuses on the northern hemisphere. The top panel shows the average scene brightness temperature measured by the CrIS sensors and highlights how the comparison dataset is characterized by extreme cold scenes, which as has been shown are associated with larger polarization corrections. The bottom panel shows the total effect of the polarization correction on the subset of CrIS data used in the comparison. For this dataset, the correction reduces the CrIS brightness temperature across the spectrum and in the shortwave band has a larger effect on SNPP CrIS than on NOAA-20 CrIS. In the midwave band, the reverse is generally true, where the polarization correction changes the NOAA-20 CrIS brightness temperature measurement more than it does for SNPP CrIS. At the scale shown, the correction does not have a noticeably different effect on SNPP or NOAA-20 in the longwave band.

The second and third panels from the top in Figure 24 show that for each of the NOAA-20 CrIS minus IASI-B and SNPP CrIS minus IASI-B differences, the polarization correction moves the bias more negative (as expected since the correction reduces CrIS measured brightness temperature), and depending on the wavenumber region, this change either increases or decreases the level of qualitative agreement between CrIS and IASI. Most notably the CrIS and IASI-B bias is moved closer to zero in the shortwave region. The second panel from the bottom shows the SNPP minus NOAA-20 CrIS bias as estimated via a double difference using IASI-B as the transfer standard. There is notable improvement in the consistency between SNPP and NOAA-20 CrIS measurements in the shortwave region and the polarization correction decreases the CrIS minus CrIS difference by up to 0.1 K and closer to zero. The longwave and midwave regions appear to be largely unaffected at the 0.1 K brightness temperature scale.

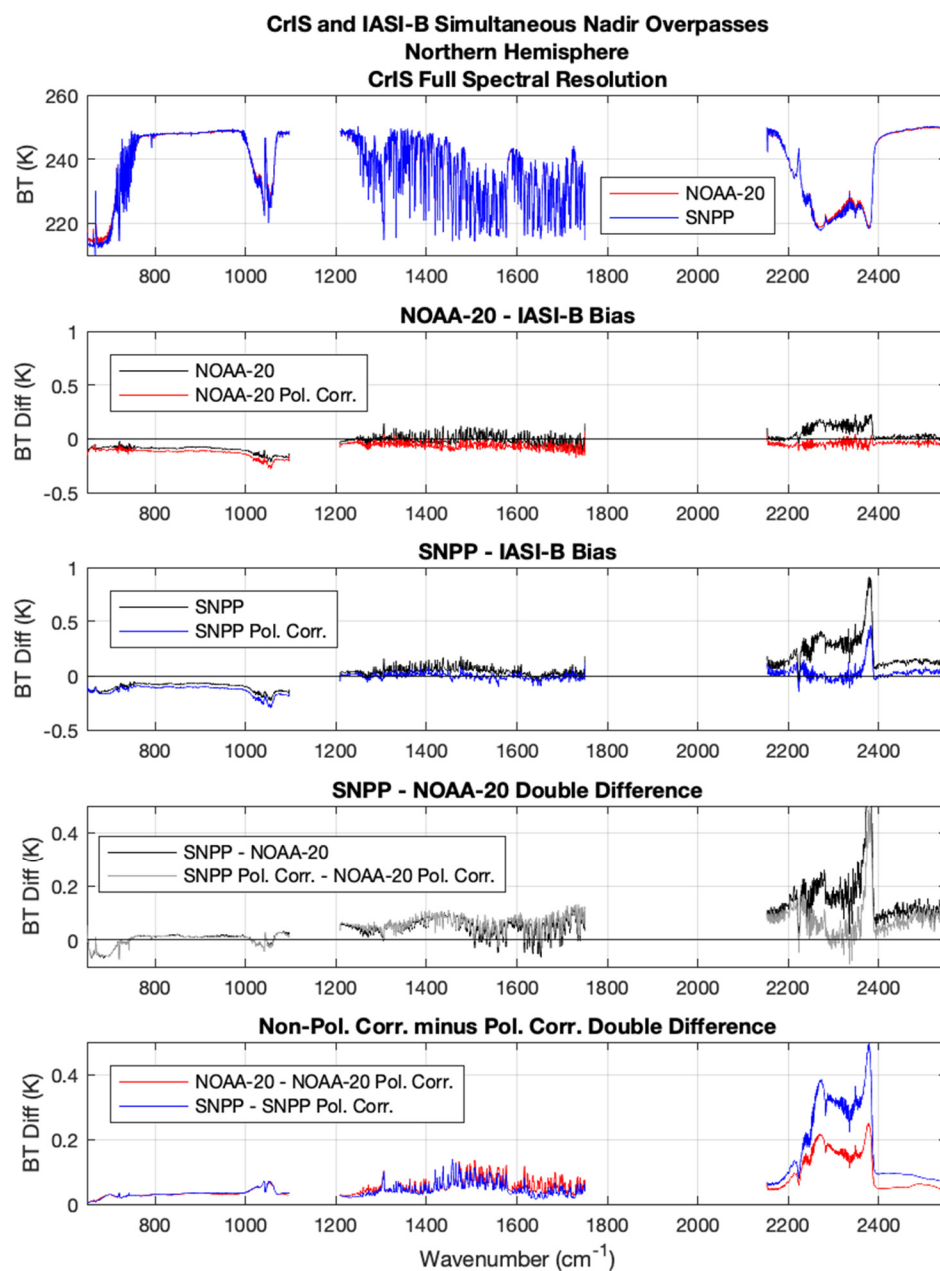


Figure 24. The impact of polarization correction on a comparison of each SNPP and NOAA-20 CrIS with METOP-B IASI. The top panel shows the mean scene brightness temperature measured by NOAA-20 and SNPP CrIS. The second and third panels from the top show the CrIS—IASI-B differences, for NOAA-20 and SNPP CrIS, respectively, and the (SNPP CrIS—IASI-B)—(NOAA-20 CrIS—IASI-B) double difference is provided in the fourth panel from the top. The bottom panel shows the total effect of the polarization correction on the subset of CrIS data used in the comparison.

7. Summary

This paper provided an overview of the view angle-dependent radiometric bias associated with polarization for the CrIS sensor. While the CrIS sensor utilizes an unprotected gold scene select mirror which has extremely low polarization in the infrared and the angle of incidence at the mirror is maintained for all calibration and scene views, there is a radiometric bias due to polarization effects, which, when uncorrected in calibration, is still non-negligible, especially for cold Earth scenes. A model for the polarization-induced radiometric bias and an associated calibration correction for the CrIS sensor was presented, along with details of the model parameter determination, and the impact of the correction

on the calibrated radiances for a range of scene temperatures and types. The effects of the polarization correction on comparisons between SNPP and NOAA-20 CrIS with one another, and with IASI-B were also provided.

As a result of this work, polarization correction was added to both the NOAA IDPS (Block 2.1 Mx8 and later) and NASA L1b (version 3 and later) calibration algorithms. Updates to the radiometric uncertainty estimate for the CrIS sensor to include the contribution associated with the uncertainty in the polarization correction were made, and were presented herein. This paper showed that the on-orbit pitch maneuver provides an extremely valuable dataset for direct derivation of the CrIS polarization parameters on-orbit. A pitch maneuver is planned to be conducted during the on-orbit intensive calibration and validation (ICV) phase of the integrated mission timelines (IMT) for NOAA-21 (JPSS-2) through NOAA-23 (JPSS-4), and will be used to derive the polarization parameters for the CrIS sensors on those platforms. Furthermore, it could be useful to include a pitch maneuver during the decommissioning for each satellite. This would allow an end-of-life assessment of the polarization parameters to be repeated for each CrIS sensor and could be used to assess if there were any significant changes in those parameters over the lifetime of the instrument.

Author Contributions: For this research, the following represents author contributions to this manuscript. Conceptualization, H.E.R., J.K.T. and D.C.T.; data curation, J.K.T. and D.C.T.; methodology, J.K.T., H.E.R. and D.C.T.; formal analysis, J.K.T., H.E.R. and D.C.T.; investigation, J.K.T., H.E.R., D.C.T., G.W., R.M., L.S., Y.C., J.P., R.O.K. and M.L.L.; writing—original draft preparation, J.K.T. and D.C.T.; writing—review and editing, J.K.T., H.E.R., D.C.T., R.O.K., M.L.L., R.M., L.S., F.I.-S., Y.C., J.P. and D.G.J.; funding acquisition, J.K.T., D.C.T. and H.E.R.; project administration, D.C.T., F.I.-S. and D.G.J. All authors have read and agreed to the published version of the manuscript.

Funding: This research was supported by the National Oceanic and Atmospheric Administration Cooperative Institute for Meteorological Satellite Studies Cooperative Agreement (current Grant NA20NES4320003) and the National Aeronautics and Space Administration support for the development of the CrIS NASA L1b product (current Grant 80NSSC22K0713) at the Space Science and Engineering Center, University of Wisconsin–Madison, Madison, WI, USA.

Data Availability Statement: The CrIS pitch maneuver data presented in this study are available on request from the corresponding author. The data were collected during on-orbit commissioning of the sensor and are not publicly available as part of the operational sensor records.

Acknowledgments: The authors would like to recognize and thank all the team members of NOAA CrIS SDR calibration and validation team and the NASA L1b calibration team for their valuable support, discussions, and suggestions. The scientific results and conclusions, as well as any views or opinions expressed herein, are those of the author(s) and do not necessarily reflect those of NASA, NOAA, or the Department of Commerce.

Conflicts of Interest: The authors declare no conflict of interest.

References

1. Eresmaa, R.; Letertre-Danczak, J.; Lupu, C.; Bormann, N.; McNally, A.P. The assimilation of Cross-track Infrared Sounder radiances at ECMWF. *Q. J. R. Meteorol. Soc.* **2017**, *143*, 3177–3188. [[CrossRef](#)]
2. Knight, E.; Merrow, C.; Salo, C. *Interaction between Polarization and Response vs. Scan Angle in the Calibration of Imaging Radiometers*; SPIE: Bellingham, WA, USA, 1999; Volume 3754.
3. Pagano, T.; Aumann, H.; Overoye, K.; Giglioli, G. *Scan-Angle-Dependent Radiometric Modulation Due to Polarization for the Atmospheric Infrared Sounder (AIRS)*; SPIE: Bellingham, WA, USA, 2000; Volume 4135.
4. Shaw, J.A. The effect of instrument polarization sensitivity on sea surface remote sensing with infrared spectroradiometers. *J. Atmos. Ocean. Technol.* **2002**, *19*, 820–827.
5. Sun, J.Q.; Xiong, X. MODIS polarization-sensitivity analysis. *Geosci. Remote Sens. IEEE Trans.* **2007**, *45*, 2875–2885.
6. Young, J.; Knight, E.; Merrow, C. *MODIS Polarization Performance and Anomalous Four-Cycle Polarization Phenomenon*; SPIE: Bellingham, WA, USA, 1998; Volume 3439.
7. Tobin, D.; Revercomb, H.; Knuteson, R.; Taylor, J.; Best, F.; Borg, L.; DeSlover, D.; Martin, G.; Buijs, H.; Esplin, M.; et al. Suomi-NPP CrIS radiometric calibration uncertainty. *J. Geophys. Res. Atmos.* **2013**, *118*, 10589–510600. [[CrossRef](#)]
8. Hecht, E. *Optics*, 4th ed.; Addison Wesley: Boston, MA, USA, 2002.
9. Collett, E. *Field Guide to Polarization*; SPIE Press: Bellingham, WA, USA, 2005; Volume 15.

10. Goldstein, D. *Polarized Light*; Marcel Dekker: New York, NY, USA, 2003; Volume 2003, p. 1.
11. Revercomb, H.E. *Polarization Effects: Theory and Characterization for Correction*; Space Science and Engineering Center, University of Wisconsin–Madison: Madison, WI, USA, 2013; pp. 1–3.
12. Taylor, J.K. *Achieving 0.1 K Absolute Calibration Accuracy for High Spectral Resolution Infrared and Far Infrared Climate Benchmark Measurements*; Université Laval: Québec, QC, Canada, 2014.
13. Aumann, H.; Gaiser, S.; Ting, D.; Manning, E. *AIRS Algorithm Theoretical Basis Document Level 1B Part 1: Infrared Spectrometer*; OS Project Science Office, NASA Goddard Space Flight Center: Greenbelt, MD, USA, 1999.
14. Revercomb, H.E.; Buijs, H.; Howell, H.B.; LaPorte, D.D.; Smith, W.L.; Stromovsky, L.A. Radiometric calibration of IR Fourier transform spectrometers: Solution to a problem with the High-Resolution Interferometer Sounder. *Appl. Opt.* **1988**, *27*, 3210–3218. [[PubMed](#)]
15. Iturbide-Sanchez, F. *Joint Polar Satellite System (JPSS) Cross Track Infrared Sounder (CrIS) Sensor Data Records (SDR) Algorithm Theoretical Basis Document (ATBD) for Full Spectral Resolution*; JPSS Configuration Management Office: Greenbelt, MD, USA, 2018.
16. Taylor, J.; Revercomb, H.; Best, F.; Gero, P.J.; Genest, J.; Buijs, H.; Grandmont, F.; Tobin, D.; Knuteson, R. *The University of Wisconsin Space Science and Engineering Center Absolute Radiance Interferometer (ARI): Instrument Overview and Radiometric Performance*; SPIE: Bellingham, WA, USA, 2014; Volume 9263.
17. Taylor, J.K.; Revercomb, H.E.; Best, F.A.; Tobin, D.C.; Gero, P.J. The Infrared Absolute Radiance Interferometer (ARI) for CLARREO. *Remote Sens.* **2020**, *12*, 1915. [[CrossRef](#)]
18. Butler, J.J.; Xiong, X.; Barnes, R.A.; Patt, F.S.; Sun, J.; Chiang, K. An overview of Suomi NPP VIIRS calibration maneuvers. In *Earth Observing Systems XVII*; SPIE: Bellingham, WA, USA, 2012; p. 85101.

Disclaimer/Publisher’s Note: The statements, opinions and data contained in all publications are solely those of the individual author(s) and contributor(s) and not of MDPI and/or the editor(s). MDPI and/or the editor(s) disclaim responsibility for any injury to people or property resulting from any ideas, methods, instructions or products referred to in the content.